CEAS Aeronautical Journal (2025) 16:641–660
https://doi.org/10.1007/s13272-025-00830-5

ORIGINAL PAPER

Performance evaluation approach for design space explorations of propulsive fuselage aircraft concepts

Nicolas G. M. Moirou[1] · **Drewan S. Sanders**[1]

Received: 23 October 2024 / Revised: 18 January 2025 / Accepted: 5 March 2025 / Published online: 1 April 2025
© The Author(s) 2025

Abstract

A promising architecture to enhance the performance of next-generation commercial aircraft involves embedding the propulsion system within the airframe, thereby capturing energy from the fuselage through boundary layer ingestion. However, in cases of strong aerodynamic coupling, traditional accounting methods break down, necessitating alternative approaches. The lack of consensus surrounding the interpretation and quantification of these benefits underscores the need for a unified assessment method. In this work, commonly used *near-field* momentum-based bookkeeping schemes are discussed and unified with a more holistic energy-based approach to evaluate aero-propulsive performance and facilitate more intuitive physical interpretations of the aerodynamics. The contribution of this work lies in the correction of the power balance, leading to the development of new metrics for assessing the efficiencies of both the aircraft and the boundary layer ingestion propulsion system. Notably, a surrogate for propulsive efficiency and limits to the power saving coefficient are given, which address inconsistencies present in the literature. Despite their application to an axi-symmetric propulsive fuselage, the metrics introduced are applicable to higher levels of representativity of propulsive fuselage concepts. The potential impact of this work is the transformation of established evaluation practices by employing these newly introduced metrics to assess aircraft and system efficiencies.

Keywords Boundary layer ingestion · Computational fluid dynamics · Performance accounting · Propulsive fuselage concept

List of symbols

C_f	Skin-friction coefficient (–)
C_p	Pressure coefficient (–)
$\dot{\mathcal{E}}_k$	Kinetic energy deposition rate (J s^{-1})
$\dot{\mathcal{E}}_p$	Rate of pressure-defect work (J s^{-1})
$\dot{\mathcal{E}}_w$	Lateral wave-outflow deposition rate (J s^{-1})
$\dot{\mathcal{E}}_\tau$	Rate of viscous boundary work (J s^{-1})
$\mathcal{F}$	Force vector (N)
$\boldsymbol{f}$	Volume-specific body force vector (N m^{-3})
FSC	Fuel saving coefficient (–)
H_0	Total enthalpy (J)
h	Mass-specific enthalpy (J kg^{-1})
h_f	Fuel heating value (J kg^{-1})
k_t	Thermal conductivity (W m^{-1} K^{-1})
L	Length (m)
M_B	Flight Mach number (–)
$\dot{m}$	Mass-flow rate (kg s^{-1})
$\dot{m}_f$	Fuel-flow rate (kg s^{-1})
$\hat{n}$	Unit normal vector
P	Total pressure (Pa)
$\mathcal{P}_f$	Propulsor body force power (J s^{-1})
$\mathcal{P}_K$	Propulsor net mechanical energy flow rate (J s^{-1})
$\mathcal{P}_K^*$	Corrected propulsor net mechanical energy flow rate (J s^{-1})
$\mathcal{P}_S$	Propulsor shaft power (J s^{-1})
PER	Potential for energy recovery (–)
PER_cc	Potential for energy recovery with compressibility correction (–)
PFS	Propulsive force share (–)
PPSC	Potential (maximum) power saving coefficient (–)
PSC	Power saving coefficient (–)
$\mathrm{PSC}_\mathrm{min}$	Minimum power saving coefficient (–)
p	Static pressure (Pa)
p_G	Gage static pressure (Pa)
R	Radius (m)
$\mathcal{S}$	Control surface (m^2)

✉ Nicolas G. M. Moirou
nicolas.g.moirou@cranfield.ac.uk

[1] Centre for Propulsion and Thermal Power Engineering, Cranfield University, Cranfield, Bedfordshire MK43 0AL, UK

s	Mass-specific entropy ($\mathrm{J\,kg^{-1}\,K^{-1}}$)
T	Static temperature (K)
$\mathcal{V}$	Control volume (m^3)
$\boldsymbol{V}$	Velocity vector in the absolute reference frame, $\boldsymbol{V} = u_i\boldsymbol{i} + u_j\boldsymbol{j} + u_k\boldsymbol{k}$ ($\mathrm{m\,s^{-1}}$)
$\boldsymbol{V}'$	Velocity vector in the relative reference frame ($\mathrm{m\,s^{-1}}$)
$\mathcal{W}$	Work (J)
γ	Specific heat ratio (–)
ε	Error related to the CFD convergence strategy (%)
Θ	Rate of volumetric pressure work ($\mathrm{J\,s^{-1}}$)
κ^*	Propulsive efficiency surrogate (–)
μ	Effective dynamic viscosity (Pa s)
ρ	Density ($\mathrm{kg\,m^{-3}}$)
$\overline{\overline{\tau}}$	Viscous stress tensor (Pa)
Φ	Rate of volumetric viscous dissipation ($\mathrm{J\,s^{-1}}$)
Φ^*	Total mechanical energy loss rate ($\mathrm{J\,s^{-1}}$)
ϕ	Rate of volume-specific viscous dissipation ($\mathrm{J\,s^{-1}\,m^{-3}}$)

Sub-/super-scripts

$(\,)_\infty$	Free-stream quantity
$(\,)_{\mathrm{A/C}}$	Quantity on aircraft
$(\,)_{\mathrm{B}}$	Quantity on body surface
$(\,)_{\mathrm{BLI}}$	Boundary layer ingesting assembly
$(\,)_{\mathrm{FE}}$	Quantity on fan-exit surface
$(\,)_{\mathrm{FF}}$	Quantity on fan-face surface
$(\,)_{\mathrm{fus}}$	Quantity on fuselage
$(\,)_{\mathrm{imb}}$	Imbalance quantity
$(\,)_{\mathrm{P}}$	Quantity on propulsor
$(\,)_{\mathrm{ref}}$	Reference fuselage/aircraft
$(\,)_{\mathrm{rev,irr}}$	Reversible, and irreversible, quantity

1 Introduction

Over the years, the position, size, and shape of aero-engines have evolved to accommodate more capable and powerful designs. To further improve propulsive efficiency, turbofans were introduced, ingesting larger mass flows and reducing specific thrust, but this also led to larger engine sizes. Despite continuous advancements, current aircraft configurations are nearing their performance limits [1], and more innovative approaches are therefore required. Distributed propulsion systems offer a complementary solution by achieving an equivalent bypass ratio (eBPR), whilst disruptive aircraft concepts aim to increase the lift-to-drag ratio and reduce aircraft weight [2]. Additionally, synergies between the airframe and engines are explored through boundary layer ingestion (BLI), which necessitates a more integrated aircraft design. Amongst the various BLI concepts [3], the propulsive fuselage concept (PFC) modifies conventional tube-and-wing designs by integrating an additional propulsor into the fuselage tail-cone.

However, novel architectures like these complicate the distinction between thrust and drag due to the close aerodynamic coupling between the propulsion system and airframe. Traditional drag definitions, based on the d'Alembert paradox and Prandtl's extension, assume inviscid and viscous flow comparisons, but in highly integrated designs, the viscous layer along the fuselage becomes significant. This influences the streamtube shapes and the forces they experience, making conventional thrust and drag book-keeping schemes less reliable [4, 5]. Recent momentum-based approaches attempt to address this [6–8], whilst energy-based methods evaluate the performance of coupled airframe-propulsion systems relative to a baseline, offering insights into BLI mechanisms and force ambiguities [9–11]. This work adopts the absolute reference frame (ARF), which views the aircraft as displacing its surrounding atmosphere through work done by the no-slip condition along its surfaces, transferring energy to the flow [9, 12]. This contrasts with the conventional relative reference frame (RRF), which considers the flow moving around a stationary aircraft.

A further challenge arises in defining propulsive efficiency for BLI systems, where values above 100% are theoretically possible. As an alternative, the power saving coefficient (PSC) was introduced by Smith Jr. [13], yet there remain inconsistencies regarding the choice of reference aircraft and engines, leading to discrepancies in PSC calculations [3]. Although the PSC is often used as a surrogate for fuel savings, it neglects key losses, such as thermal and core inefficiencies, which affect shaft power calculations as found in Refs. [14, 15].

As there is no universal metric for assessing performance, benefits can only be evaluated relative to a reference configuration. This work addresses gaps in evaluating the aero-propulsive performance of novel BLI aircraft by combining momentum and energy-based approaches for more comprehensive insights into flow mechanisms. Building on the power balance method introduced by Drela [10], this study improves the definition of propulsive efficiency in Sect. 2 by correcting for both reversible and irreversible losses in the propulsor stage. A case study of a propulsive fuselage concept is presented in Sect. 3, comparing a conventional non-BLI aircraft to its BLI derivative. The findings, which detail the actual power available for work on the fluid in Sect. 4,

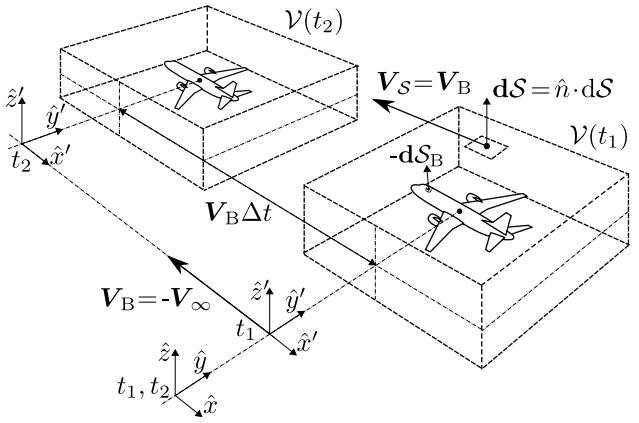


Fig. 1 Motion of a flying aircraft from t_1 to t_2 with its control volume in the ARF ($\hat{x}$, $\hat{y}$, $\hat{z}$) and the RRF ($\hat{x}'$, $\hat{y}'$, $\hat{z}'$, from Ref. [16]). *Source:* Adapted with permission from Sanders, D. S., "Aircraft Aerodynamic Work-Energy Relationships with Mass Source Considerations," Tech. Rep. RP0028, Cranfield University, Cranfield, United Kingdom, 2023

are further discussed in relation to the PSC in Sect. 5. The study highlights the origins of fuel savings and introduces metrics to address ambiguities related to reference aircraft and engines. This work has the potential to challenge conventional evaluation practices and establish universal metrics applicable to BLI-integrated aircraft.

2 Power balance on partial assemblies

2.1 Universal mechanical energy balance

2.1.1 Introduction of moving control volumes

Traditional aerodynamic analysis separates propulsion from the airframe to differentiate thrust (positive) and drag (negative) forces. This method relies on infinite streamtubes and principles like the d'Alembert paradox and Prandtl's extension to evaluate forces. In BLI aircraft, however, the propulsion system and airframe share a common streamtube, blurring the distinction between thrust and drag. To address this, energy-based methods using a RRF have been developed [10, 11]. In the RRF, the aircraft is stationary and the flow moves over it, mimicking wind-tunnel conditions. Here, propulsion offsets the airframe's momentum deficit to achieve equilibrium.

From the ARF, inconsistencies emerge: whilst no useful work is performed in the RRF due to the system's static appearance, the ARF recognises useful work as thrust power.

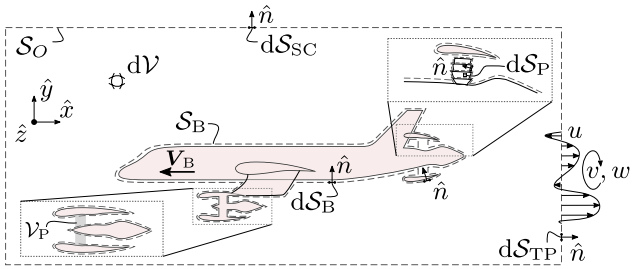


Fig. 2 Schematic of a control volume encapsulating a powered aerodynamic body

Sanders and Laskaridis [9] refined Drela's [10] power balance to resolve this, demonstrating its universality for moving control volumes [16]. Figure 1 illustrates a moving control volume (CV) around an aircraft, showing equivalence between the RRF and ARF. The aircraft features an outer surface $\mathcal{S}_B$, with infinitesimal normal surface elements $\mathbf{d}\mathcal{S} = \hat{\boldsymbol{n}}\, \mathrm{d}\mathcal{S}$ pointing inward to the body and outward along the CV, as it flies at velocity $\boldsymbol{V}_B$.

Conservation equations for mass, momentum, and energy, simplified in the RRF, are insufficient for moving CVs. Using the Leibniz-Reynolds transport theorem, these equations are adapted. When the velocity $\boldsymbol{V}_S = 0$, the ARF equations reduce to their RRF counterparts, applicable to stationary CVs.

2.1.2 Mechanical energy balance

The power balance in Eq. (1), arranged to distinguish power sources (left-hand side) and sinks (right-hand side), is applied to a propulsive fuselage aircraft. In this configuration, an aft-end thruster, turbo-electrically powered by two under-wing turbofans in a thrust-splitting architecture, supplements their propulsive force [3]. Figure 2 illustrates this setup, with the volume $\mathcal{V}$ at t_1 (from Fig. 1) bounded by a two-dimensional cutaway. The bounding surface comprises the outer surface $\mathcal{S}_O$ (side cylinder and Trefftz planes, $\mathcal{S}_O = \mathcal{S}_{SC} \cup \mathcal{S}_{TP}$) and the inner surface, split into fuselage walls $\mathcal{S}_B$ and permeable propulsive surfaces $\mathcal{S}_P$, which enclose $\mathcal{V}_P$, representing the propulsor's body forces on the flow.

To enhance physical intuition, Ref. [9] contextualises Drela's power balance [10] with energy transfer pathways in the ARF, inspired by Renard and Deck [17]. Unlike the RRF, where the atmosphere ambiguously acts as both source and sink, the ARF resolves these ambiguities using Galilean covariance (as opposed to RRF's Galilean invariance) [12] with surface forces adhering to the no-slip condition transfer energy to the flow, forming a boundary layer.

$$
\begin{aligned}
&\underbrace{-\oiint_{\mathcal{S}_\mathrm{P}} \left(p_\mathrm{G}\boldsymbol{V}'_\mathcal{S} - \bar{\bar{\tau}}\cdot\boldsymbol{V}'_\mathcal{S}\right)\cdot\,\mathrm{d}\boldsymbol{\mathcal{S}}}_{\mathcal{P}_S} + \underbrace{\iiint_\mathcal{V} \rho\boldsymbol{f}\boldsymbol{V}'\,\mathrm{d}\mathcal{V}}_{\mathcal{P}_f} + \overbrace{\underbrace{\oiint_{\mathcal{S}_\mathrm{B}} \left(p_\mathrm{G}\boldsymbol{V}_\mathrm{B} - \bar{\bar{\tau}}\cdot\boldsymbol{V}_\mathrm{B}\right)\cdot\,\mathrm{d}\boldsymbol{\mathcal{S}}}_{-\mathcal{F}_\mathbf{B}\cdot\boldsymbol{V}_\mathbf{B}} + \underbrace{\iiint_\mathcal{V} \rho\boldsymbol{f}\boldsymbol{V}_\mathrm{B}\,\mathrm{d}\mathcal{V}}_{-\mathcal{F}_f\cdot\boldsymbol{V}_\mathbf{B}}}^{-W\dot{h}} = \ldots \\
&\qquad\qquad \underbrace{-\oiint_{\mathcal{S}_O} \rho\frac{\boldsymbol{V}^2}{2}\boldsymbol{V}' + p_\mathrm{G}\boldsymbol{V} - \bar{\bar{\tau}}\cdot\boldsymbol{V}\cdot\,\mathrm{d}\boldsymbol{\mathcal{S}}}_{\dot{\mathcal{E}}} + \underbrace{\iiint_\mathcal{V} -p_\mathrm{G}\nabla\cdot\boldsymbol{V}\,\mathrm{d}\mathcal{V}}_{\Theta} + \underbrace{\iiint_\mathcal{V} \left(\bar{\bar{\tau}}\cdot\nabla\right)\cdot\boldsymbol{V}\,\mathrm{d}\mathcal{V}}_{\Phi}
\end{aligned}
\tag{1}
$$

2.1.3 Propulsor mechanical power caveat

Shaft power ($\mathcal{P}_S$) relates to the work done by a moving fan's blades on the flow relative to the body (top-right corner in Fig. 2), corresponding to a rise in total enthalpy ($\mathcal{P}_S = -\Delta H_0$). The term $\mathcal{P}_f$, from Eq. (1), represents a body force across a volume (bottom-left in Fig. 2) and is equivalent to $\mathcal{P}_S$ and the total enthalpy rise. This approach is preferred in early-stage designs when the propulsor geometry is unknown [15, 18, 19], whilst $\mathcal{P}_S$ is used when the propulsor is modelled with inlet/outlet boundary conditions [14, 20, 21].

Both $\mathcal{P}_S$ and $\mathcal{P}_f$ differ from $\mathcal{P}_K$, the power crossing the fan's inlet and outlet surfaces. $\mathcal{P}_K$, denoting the additional energy deposition rate, represents the mechanical energy flux change across these stations [10, 22–24]. However, unlike total enthalpy rise, $\mathcal{P}_K$ depends on the location of the inlet and outlet boundaries because it includes pressure-volume work (Θ_P) within the fan's volume ($\mathcal{V}_\mathrm{P}$). Using the mechanical energy conservation equation in the ARF and comparing it with the total energy equation, the non-equivalence between these power sources is given in Eq. (2).

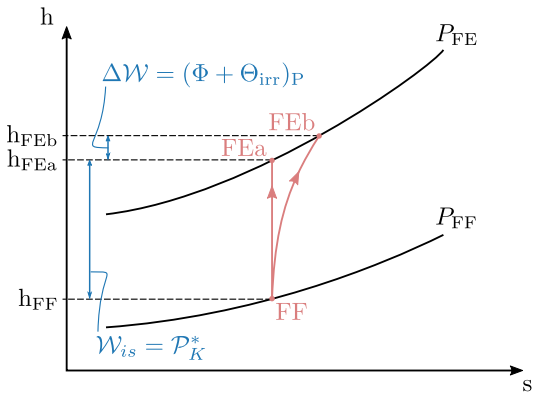


Fig. 3 Enthalpy–entropy diagram for a compressor stage between its fan-face (FF) and fan-exit (FE) stations

2.1.4 Work-energy transfers in flight

The potential energy rate ($W\dot{h}$) accounts for changes in altitude ($\dot{h}$), where power excess or deficit leads to climb or descent. This potential energy rate represents the

$$
\underbrace{-\oiint_{\mathcal{S}_\mathrm{P}} \left(p_\mathrm{G}\boldsymbol{V}'_\mathcal{S} - \bar{\bar{\tau}}\cdot\boldsymbol{V}'_\mathcal{S}\right)\cdot\,\mathrm{d}\boldsymbol{\mathcal{S}}}_{\mathcal{P}_S} = \underbrace{\oiint_{\mathcal{S}_O} \left(\rho\frac{\boldsymbol{V}^2}{2}\boldsymbol{V}' + p_\mathrm{G}\boldsymbol{V} - \overset{\approx 0}{\cancel{\bar{\bar{\tau}}}}\cdot\boldsymbol{V}\right)\cdot\,\mathrm{d}\boldsymbol{\mathcal{S}}}_{\mathcal{P}_K} + \underbrace{\iiint_{\mathcal{V}_\mathrm{P}} -p_\mathrm{G}\nabla\cdot\boldsymbol{V}'_\mathcal{S}\,\mathrm{d}\mathcal{V}}_{\Theta_\mathrm{P}} + \underbrace{\iiint_{\mathcal{V}_\mathrm{P}} \left(\bar{\bar{\tau}}\cdot\nabla\right)\cdot\boldsymbol{V}'_\mathcal{S}\,\mathrm{d}\mathcal{V}}_{\Phi_\mathrm{P}}
\tag{2}
$$

Further, the rate of pressure work within the fan volume Θ_P is composed of isentropic (reversible, $\Theta_{\mathrm{rev,P}}$) and non-isentropic (irreversible,[1] $\Theta_{\mathrm{irr,P}}$) components that can subsequently be identified in Eq. (3).

$$
\mathcal{P}_S \equiv \mathcal{P}_f \equiv \Delta H_0 \equiv \mathcal{P}_K + \Theta_\mathrm{P} + \Phi_\mathrm{P} = \underbrace{\mathcal{P}_K + \Theta_{\mathrm{rev,P}}}_{\mathcal{P}^*_K} + \underbrace{\Phi_\mathrm{P} + \Theta_{\mathrm{irr,P}}}_{\Phi^*_\mathrm{P}}
\tag{3}
$$

pseudo-work of forces acting on the flow. Mechanical energy fluxes $\dot{\mathcal{E}}$) across the outer boundary surface ($\mathcal{S}_O$) are decomposed into side cylinder ($\dot{\mathcal{E}}_{\mathrm{SC}}$) and Trefftz plane ($\dot{\mathcal{E}}_{\mathrm{TP}}$) surfaces, as shown in Fig. 2. These fluxes include wake streamwise kinetic energy ($\dot{\mathcal{E}}_u$), transverse kinetic energy ($\dot{\mathcal{E}}_v$), wake pressure-defect work ($\dot{\mathcal{E}}_p$), viscous boundary work ($\dot{\mathcal{E}}_\tau$), and wave-outflow energy ($\dot{\mathcal{E}}_w$). Combined, $\dot{\mathcal{E}}_u$ and $\dot{\mathcal{E}}_v$ form $\dot{\mathcal{E}}_k$, representing the overall wake kinetic energy rate.

[1] This term echoes the baroclinic power from Sato [25] imparted to the flow and due to non-isentropic compression and dilation waves encountered in transonic compressible flows.

$$\dot{\mathcal{E}} = \overbrace{\underbrace{\iint_{\mathcal{S}_{\mathrm{TP}}} \left(\frac{\rho}{2}\boldsymbol{V}^2\right)\boldsymbol{V}' \cdot \hat{n}\,\mathrm{d}\mathcal{S}}_{\dot{\mathcal{E}}_k} + \underbrace{\iint_{\mathcal{S}_{\mathrm{TP}}} p_{\mathrm{G}}\boldsymbol{V} \cdot \hat{n}\,\mathrm{d}\mathcal{S}}_{\dot{\mathcal{E}}_p} + \underbrace{\iint_{\mathcal{S}_{\mathrm{TP}}} -\bar{\bar{\tau}} \cdot \boldsymbol{V} \cdot \hat{n}\,\mathrm{d}\mathcal{S}}_{\dot{\mathcal{E}}_\tau}}^{\dot{\mathcal{E}}_{\mathrm{TP}}}$$
$$+ \overbrace{\underbrace{\iint_{\mathcal{S}_{\mathrm{SC}}} \left[\left(\frac{\rho}{2}\boldsymbol{V}^2\right)\boldsymbol{V}' + p_{\mathrm{G}}\boldsymbol{V} - \bar{\bar{\tau}} \cdot \boldsymbol{V}\right] \cdot \hat{n}\,\mathrm{d}\mathcal{S}}_{\dot{\mathcal{E}}_w}}^{\dot{\mathcal{E}}_{\mathrm{SC}}} \tag{4}$$

At sufficiently distant boundaries (SC and TP), only excess energy fluxes are captured, as these surfaces remain unaffected by flow perturbations. Energy deposited within the flow volume ($\mathcal{V}$) converts into sinks Φ and Θ as the flow dissipates to a quiescent state. The term Θ quantifies volumetric pressure work due to compression and dilation waves against atmospheric pressure, analogous to Drela's power balance term $\mathcal{P}_V$, with its sign indicating power loss from non-isentropic compressibility effects [25]. The term Φ measures viscous dissipation along the flow path, representing irreversible mechanical losses as heat.

2.1.5 Fan isentropic efficiency

Fan efficiency (η_{fan}) is defined as the ratio of isentropic work ($\mathcal{W}_{is}$) to actual work ($\mathcal{W}_a$) and distinguishes $\mathcal{P}_K$ from $\mathcal{P}_S$ (or $\mathcal{P}_f$). Isentropic work represents the energy available for flow work, excluding intrinsic losses. The enthalpy-entropy diagram in Fig. 3 illustrates the rise in total pressure across a fan stage, highlighting changes in enthalpy and entropy. The corrected additional power ($\mathcal{P}_K^*$) corresponds to the reversible portion of work, as derived in Eq. (3).

Fan isentropic efficiency (η_{fan}) is approximated by Eq. (5) when the control volume ($\mathcal{V}_{\mathrm{P}}$) closely envelops the fan's geometry, boundary layers, and shock structures, with inlet and outlet interfaces positioned near the fan, as in Fig. 2. This efficiency also allows for the deduction of $\Theta_{\mathrm{rev,P}}$. Whilst total irreversible losses in the fan ($\Theta_{\mathrm{irr,P}}$ and Φ_{P}) cannot be separated, they can still be quantified. This decomposition significantly improves the balance of power terms, influencing the useful work available for the flow.

$$\eta_{\mathrm{fan}} = \frac{\mathcal{P}_K^*}{\mathcal{P}_S} = \frac{\mathcal{P}_K + \Theta_{\mathrm{rev,P}}}{\mathcal{P}_S} = 1 - \frac{\left(\Theta_{\mathrm{irr}} + \Phi\right)_{\mathrm{P}}}{\mathcal{P}_S} \tag{5}$$

2.2 Application to decoupled aero-propulsive partial assemblies

To simplify the analysis, one can crudely assume weak aerodynamic coupling between the fuselage assembly (fuselage and thruster) and the remaining aerodynamic components (wings, pylons, under-wing engines and vertical and horizontal tail planes) via an approach similar to a drag build-up method (Fig. 4). In doing so, the fuselage/thruster assembly experiences a net force imbalance $\boldsymbol{\mathcal{F}}_{\mathrm{imb}}$, even in steady-level flight condition, which must be accounted for within the energy balance. The imbalance experienced by the partial assembly is comprised of two contributions given in Eq. (6) with a change in potential energy of the sub assembly and the force power of the rest of the components decoupled from the assembly. Therefore, the previous imbalance suggested by $(W\dot{h})_{\mathrm{net}}$ lumps together $(W\dot{h})_{\mathrm{fus+P}}$ for the simplified assembly, and $\boldsymbol{\mathcal{F}}_{\mathrm{rest}} \cdot \boldsymbol{V}_{\mathrm{B}}$ for the remaining components.

$$\begin{aligned}(W\dot{h})_{\mathrm{net}} = \left(\boldsymbol{\mathcal{F}}_{\mathrm{imb}} \cdot \boldsymbol{V}_{\mathrm{B}}\right) &\overset{?}{=} (W\dot{h})_{\mathrm{fus+P}} + (W\dot{h})_{\mathrm{rest}} \\ &\overset{?}{=} (\boldsymbol{\mathcal{F}}_{\mathrm{fus}} + \boldsymbol{\mathcal{F}}_{\mathrm{P}}) \cdot \boldsymbol{V}_{\mathrm{B}} + \boldsymbol{\mathcal{F}}_{\mathrm{rest}} \cdot \boldsymbol{V}_{\mathrm{B}}\end{aligned} \tag{6}$$

This formulation becomes advantageous as it simplifies a problem by isolating a system, and its performance evaluation. To that end, $\boldsymbol{\mathcal{F}}_{\mathrm{imb}}$ is quantified with an explicit formulation of forces imbalance over partial assemblies (fuselage, $\boldsymbol{\mathcal{F}}_{\mathrm{fus}}$, and BLI propulsor, $\boldsymbol{\mathcal{F}}_{\mathrm{P}}$), and proves its usefulness when thrust-splitting architectures are considered to deduce the remaining force necessary by the under-wing engines to maintain the net change in potential energy of the entire aircraft. In these scenarios, the energy balance in Eq. (1) reduces to Eq. (7) where the net potential energy change is substituted with its sub-assembly quantity, related to an imbalance force.

$$\mathcal{P}_S + \mathcal{P}_f - (\boldsymbol{\mathcal{F}}_{\mathrm{fus}} + \boldsymbol{\mathcal{F}}_{\mathrm{P}}) \cdot \boldsymbol{V}_{\mathrm{B}} = (W\dot{h})_{\mathrm{rest}} + \dot{\mathcal{E}} + \Phi + \Theta \tag{7}$$

3 Propulsive fuselage aircraft design

3.1 Reference state-of-the-art aircraft

3.1.1 Airframe outer outline

From the assumption of weak aerodynamic coupling [26] between the fuselage and the rest of the airframe of a medium-range single-aisle aircraft, a simplified two-dimensional (2D) axi-symmetric fuselage is derived [27]. A drag build-up approach [28, 29] relates the isolated fuselage to the entire vehicle. The fuselage chord L_{fus} is segmented in three distinct parts: an ellipsoidal nose, a cylinder of constant radius R_{fus} for the cabin and a conical tail. Although

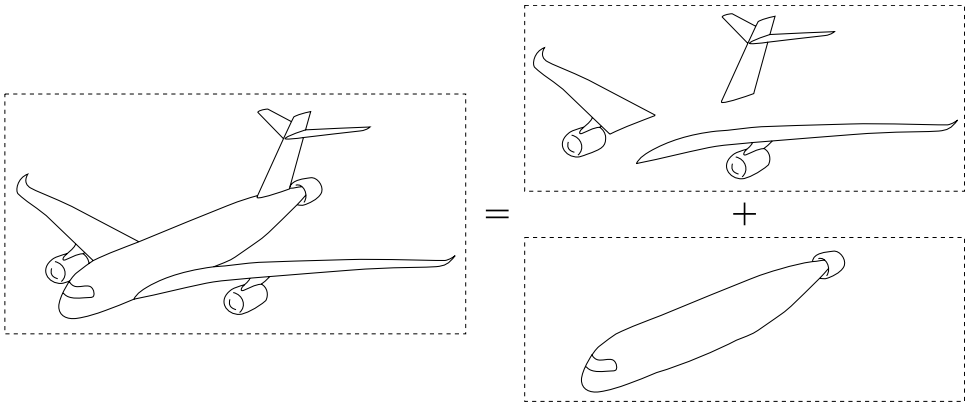


Fig. 4 Decomposition of the propulsive fuselage concept into partial assemblies

it is common to consider a frustum to represent the aircraft tail, a cone is favoured in this approach to prevent singularities in the mesh and potential flow recirculation behind the vehicle.

3.1.2 Under-wing engines

Two state-of-the-art turbofans (TF) mounted under the wings of the reference single-aisle aircraft ensure a constant vehicle speed V_B at cruise (for a given altitude, drag coefficient and engine operating conditions). The two-spool architecture developed by Zhao and Yao [30] is composed of an 11:1 by-pass ratio single-stage fan of pressure ratio 1.49, 3-stage intermediate-pressure and 10-stage high-pressure compressor, and 2-stage high-pressure and 7-stage low-pressure turbine for an overall pressure ratio of 44. The free-stream conditions are defined following the International Standard Atmosphere (ISA) model based on the cruise altitude and Mach number, and assuming isentropic inflow conditions. The engine performance is evaluated at on-design from which a nacelle drag estimation sub-process determines the nacelle drag based on the flight conditions [31]. The drag build-up and nacelle drag estimation help determine an installed thrust-specific fuel consumption used as reference for comparison.

3.2 Propulsive fuselage aircraft

To attenuate the aircraft wake losses, energy is harvested from the viscous layer developing around the fuselage by a BLI propulsor. Whilst a convenience exists in retrofitting a BLI propulsor around a conical tail [6], larger degrees of integration rely on a strategic tail reshaping to obtain a natural flow pre-diffusion before entering the fan. Despite the opportunity of ingesting the entire circumference of the fuselage's boundary layer flow rich in energy and subject to reasonable distortion [32], there are numerous challenges that arise on the propulsor position, size and shape, as well as the determination of the propulsor and vehicle performance.

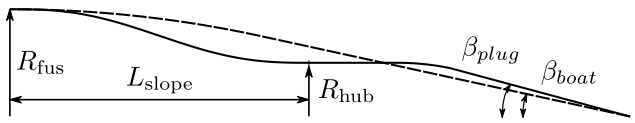


Fig. 5 Tail morphing sequence from its reference (– –) to its morphed shape (—-)

3.2.1 Fuselage tail morphing sequence

To not violate the reference geometry constraints and approximations, the propulsor must be integrated whilst ensuring a pre-diffused inflow and avoiding recirculation upstream of the nacelle. To that end, the tail is morphed with a slope towards the plug of the aircraft, where a circular arc connects to the right-angled plug of angle β_{plug} to ensure continuity and tangency (Fig. 5). In doing so, the tail-cone radius is shrunk in its middle to ensure minimal distortion, meet the Mach number target and avoid separation ahead of the propulsor intake [27]. Seeking a robust, versatile, and yet easy to implement method allowing for design space explorations, the Bell-Mehta fifth-order polynomial (Eq. (8), where $x' = x/L_{\text{slope}}$, $y_i = R_{\text{fus}}$ and $y_j = R_{\text{hub}}$) is selected for the slope parametrisation preventing any early separation (seventh-order polynomial) and non-uniformity (third-order polynomial) [33].

$$y(x) = y_i - \left(y_i - y_j\right)\left[6(x')^5 - 15(x')^4 + 10(x')^3\right] \tag{8}$$

3.2.2 Integrated aft-fuselage propulsor

Figure 6 depicts a schematic of the axi-symmetric propulsive fuselage and a zoomed-in region of the tail which features the pre-diffusive slope, the BLI propulsor and the aft-cone.

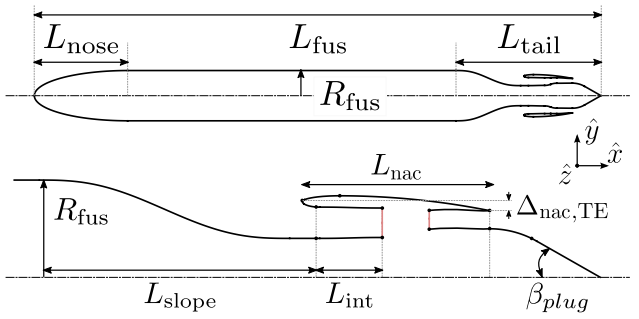


Fig. 6 Schematic of an axi-symmetric propulsive fuselage concept and its parametrisation

The outer nacelle cowl is modelled following a NACA-1 Series profile until the crest and a circular arc for the aft portion, whilst the interior intake's and exhaust's hub and shroud agree with the Bell-Mehta fifth polynomial given in Eq. (8). Further details on the entire design process and parametrisation are provided in Ref. [26]. In spite of a rather simple parametrisation that enables the applicability of the present performance assessment approach to a PFC, more complex and refined definitions from Refs. [34–37] can be used.

3.2.3 Rescaled under-wing engines

Alike the reference aircraft, a conventional kerosene-fed propulsion system is considered to propel the aircraft. Based on a turbo-electric architecture, mechanical power is extracted from the main engines' low-pressure turbines to electrically drive the aft-mounted propulsor. The latter complements the main turbofans' thrust generation to introduce a propulsive force share (PFS, detailed in Sect. 4.2). Nonetheless, the transmission system and power conversion process are not modelled in that work and the inherent losses are approximated with transmission losses given by η_{trans}. A benefit emanating from the thrust-splitting configuration is the rescaling of the turbofans as a lower thrust is required from them. To that end, the turbofan candidate selected for the reference aircraft can either be retrofitted in the PFC or scaled-down accounting for the different thrust and power off-take requirement combinations. Engine decks are therefore generated to be coupled with the aft-mounted propulsor's power requirement advising on the engines' fuel consumption [30].

3.3 Numerical set-up and implementation

3.3.1 Mesh topology

An automated structured grid generation methodology is implemented using ANSYS ICEM 20.2 [38]. All geometries are encapsulated by bullet-shape domains following a multi-block strategy. To avert flow impingements to the far-field, a coupled grid and domain convergence study following Ref. [39]'s procedure, and detailed in Appendix 1, advised on 10 fuselage chords upstream and above the body $d_{\text{far-field}}$, and a Trefftz position d_{outlet} at 40 fuselage lengths behind it. The mesh parametrisation is elaborated in a fashion that elements close to the wall ensure a fineness with a y^+ that falls between 0.9 and 1.0 along the whole body, and the grid coarsens the farther away from the vehicle to the Trefftz plane. The multi-grid structure is composed of a C-grid topology surrounding the vehicle from its centreline. In the propulsive fuselage configuration, a C-grid topology is nested within the clean mesh, i.e. mesh of the reference aircraft (Fig. 7), to refine the nacelle and propulsor region.

3.3.2 Flow solver and computational strategy

The density-based solver of ANSYS Fluent 20.2 [40] is used to perform the compressible and viscous computations by solving the Reynolds-Averaged Navier–Stokes equations in the 2D axi-symmetric domain. The far-field is represented by the circular arc and top surface of the bullet shape (Fig. 8) where a pressure far-field condition is set with $M_{\text{B}} = 0.78$ and the fuselage-length $Re = 2.73.10^8$ at ISA conditions ($\rho = 0.3807$ kg/m^3, $p = 23922$ Pa and $\mu = 1.434.10^{-5}$ kg/m/s). The flow that exits the Trefftz is defined by a pressure outlet boundary condition. A coupled pressure–velocity scheme is used where the spatial discretisation is resolved with second order Green-Gauss cell-based gradient schemes. The air travelling through the domain is modelled as an ideal gas and a no-slip condition is ensured on the walls of the aircraft where the surrounding flow is resolved using the two-equation Shear-Stress Transport (SST) k-ω turbulence model [41]. The specific heat ratio γ depends only on the temperature, with the heat capacity at constant pressure $C_p(T)$ following a second-order piecewise-polynomial function of temperature. The fluid viscosity μ is also temperature-dependent, according to the Sutherland's law.

As for the propulsion model, named expressions in Fluent are used between the fan-face and -exit 1D boundary conditions, which is an iterative procedure depicted in Fig. 9. The fan-face sees the flow leaving its surface defining an initial particular mass-flow. also regulated by the nozzle plane. Through the operating conditions at which the fan performs, isentropic relationships are used to determine the fan-exit flow conditions ensuring continuity through the propulsor stage. The pressure rise is computed and compared against used-defined target values until a certain threshold is met, otherwise the mass-flow rate obtained at the fan-exit is fed back into the fan-face through its pressure outlet condition. To ensure convergence of the propulsion model, threshold criteria are defined on the polytropic efficiency of the fan

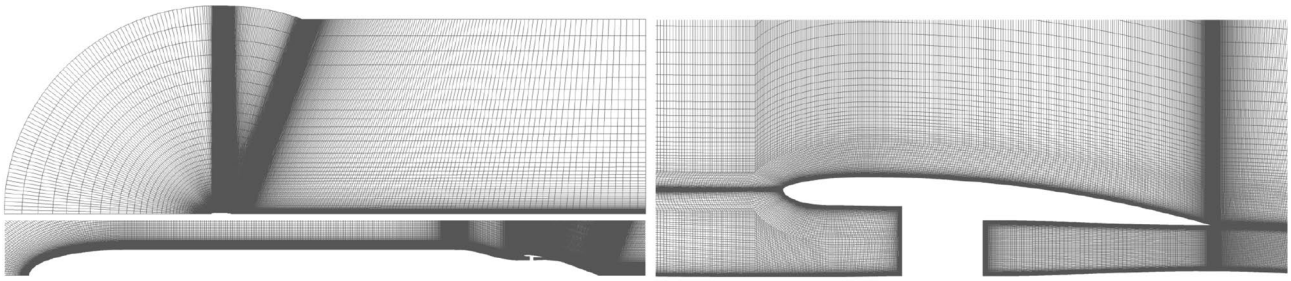


Fig. 7 C-grid around a propulsive fuselage with the domain's mesh, around the fuselage and the propulsor

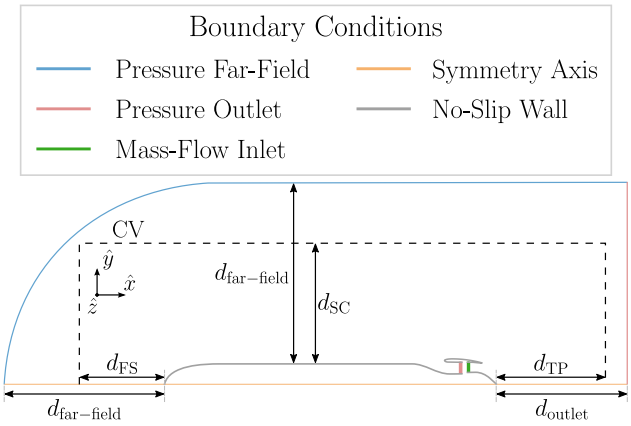


Fig. 8 Schematic of the domain, propulsive fuselage model, boundary conditions and analysis control volume

and its pressure ratio. At the fan-exit, total temperature and pressure, and polytropic efficiency are calculated until convergence which is tracked through the error, or difference, between the target and obtained fan pressure ratio (FPR), ϵ_{FPR}, target and obtained polytropic efficiency, $\epsilon_{\eta_{poly}}$, and mass imbalance through the fan, $\epsilon_{\dot{m}}$.

In addition to the propulsion model and residual convergences, *near-* and *far-field* force comparison calculations are performed. A unique control volume encapsulates the aircraft where the distances upstream d_{FS} and above d_{SC} are defined from the domain convergence study (Appendix 1), and survey transverse planes d_{TP} in the wake are swept to inquire the flow-field. In the *near-field*, pressure and shear-stress are computed along all physical surfaces. In the *far-field*, the force is extracted from energy-based integral components and both forces are iteratively compared until convergence below a certain threshold (Appendix 2).

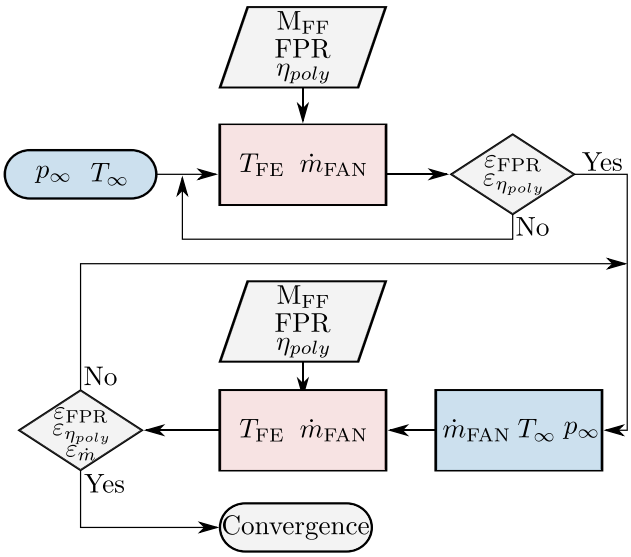


Fig. 9 Fan modelling iterative procedure within the CFD with conditions at the fan-face (blue) and fan-exit (red)

4 On-design aero-propulsive performance evaluation approach

4.1 Reference aircraft benchmarking

To assess the BLI benefits, the reference aircraft model is used as a benchmark. The fuselage stream-wise net force $\mathcal{F}_{\text{fus,ref}}$ is computed in CFD on the axi-symmetric model following Eq. (9), and is verified against a drag build-up approach, further detailed in Appendix 3, with its derived profile and induced drag components. The aircraft drag breaks down to 54.4% related to lift-independent drag, 41.8% that results from lift, and 3.8% for the wave and trim drags.

$$\mathcal{F} = \iint_{\mathcal{S}} (p - p_\infty)\hat{n} - \bar{\bar{\tau}} \cdot \hat{n} \, \mathrm{d}\mathcal{S} \tag{9}$$

The drag polars suggest that when isolating aerodynamically the bare fuselage from the rest of the airframe (alike Fig. 4), its profile drag amounts to around a quarter of the entire aircraft drag (Fig. 10). The portion of the other component's profile drag is also provided, allowing the CFD-issued fuselage stream-wise force to be used to determine

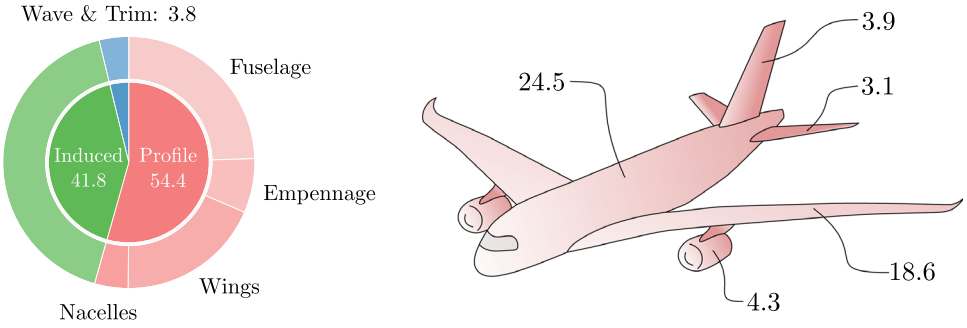


Fig. 10 Aircraft profile, lift-induced and wave drag shares (left), and aircraft components' portions of profile drag (right)

the entire aircraft's force experienced $\mathcal{F}_{\mathrm{A/C,ref}}$ under cruise conditions.

To maintain a steady cruise level, $\mathcal{F}_{\mathrm{A/C,ref}}$ is matched and split by two under-wing engines providing equal amounts of output force. The two state-of-the-art turbofans, pylon-mounted under either wings, are considered fed by kerosene which power supply is given by the product of the fuel mass-flow $\dot{m}_f$ and its heating value h_f in Eq. (10). Alternatively, in fully-electric architectures where a power source feeds the engines, an in-house propulsion model is used to determine the power consumption to generate the output force. In both scenarios, the reference aircraft power consumption serves as benchmark.

$$\mathcal{P}_{\mathrm{A/C,ref}} = \dot{m}_{f,\mathrm{A/C,ref}} \cdot h_{f,\mathrm{A/C,ref}} \tag{10}$$

4.2 Propulsive force share

The close integration of the BLI propulsor around the aircraft tail makes it challenging to isolate its positive propulsive force contribution. An alternative consists in determining the axial net force by including the BLI nacelle contribution and comparing it to the axial net force of the unpowered propulsive fuselage, without nacelle. To do so, the axial net force on the aircraft featuring the morphed tail ($\mathcal{F}_{\mathrm{fus,MOR}}$) is extracted from CFD at the same flight conditions as the powered PFC. When compared with the net axial force of the propulsive fuselage $\mathcal{F}_{\mathrm{fus+P,PFC}}$, the installed BLI propulsor propulsive force $\mathcal{F}_{\mathrm{BLI}}$ is isolated (Eq. (11)). On both morphed and propulsive fuselages, the net axial force is computed from a *near-field* integration of the local pressure and skin-friction forces (Eq. (9)). The rapidness and ease of implementation of the *near-field* integration motivates its choice over other *far-field* integration methods that have been compared in Appendix 2.

$$\mathcal{F}_{\mathrm{BLI}} = \mathcal{F}_{\mathrm{fus+P,PFC}} - \mathcal{F}_{\mathrm{fus,MOR}} \tag{11}$$

However, an assumption is taken where all changes in force between the un-installed and installed configurations of the propulsive fuselage are attributed to the propulsor integration (e.g. propulsor forward force and nacelle losses) despite the strong effect the integration has upstream along the tail [21]. This assumption is given by Eq. (11) as the resulting force between the propulsive fuselage and its clean morphed equivalent. Assuming the same drag decomposition from the aerodynamic decoupling, and lift-to-drag ratio of the reference aircraft, the propulsive fuselage aircraft entire drag $\mathcal{F}_{\mathrm{PFC}}$ is deduced.

However, to compare different PFC designs, this quantity needs to be non-dimensional as it also impacts the propulsive force requirement from the turbofans. Therefore, a propulsive force share (PFS) is defined in Eq. (12) as a means of quantifying the portion of propulsive force provided by the aft-mounted fan relative to the aircraft's overall requirement. This non-dimensional form shows its importance when one designs different aircraft and evaluates the change in propulsive force under equivalent power supply, or inversely, the change in power requirement to maintain the same force share.

$$\mathrm{PFS} = \frac{\mathcal{F}_{\mathrm{BLI}}}{\mathcal{F}_{\mathrm{PFC}}} \tag{12}$$

4.3 Propulsive efficiency surrogate

Propulsive efficiency is defined as the efficacy at which the propulsive power available is converted into useful work acting on the flow. Whilst a surrogate of this metric was offered by Sanders and Laskaridis [9] in Ref. [9] with κ, $\mathcal{P}_S$ was wrongly, but knowledgeably, used as the available power source, other studies [22, 24] used the ambiguous $\mathcal{P}_K$ term. In the former definition, losses are considered in the "available" power whereas in the latter, recoverable pressure work is omitted. Therefore, Eq. (13) offers an improvement with the correction of the denominator by considering the real power available to exert work on the flow, $\mathcal{P}^*_K$. This

provides efforts towards a *real* propulsive efficiency definition, despite remaining a surrogate of it, since the numerator is still erroneous as it does not provide a correct definition of useful work but rather a propulsive power. To meet the gap between propulsive power and useful work, one must identify the sources of losses that do not contribute to exerting work on the flow, e.g. Φ^* within the jet.

$$\kappa^* = \frac{\mathcal{F}_{\text{BLI}} \cdot \boldsymbol{V}_{\text{B}}}{\mathcal{P}_K^*}, \quad \text{where } \mathcal{P}_K^* = \eta_{fan} \cdot \mathcal{P}_{S,\text{BLI}} \tag{13}$$

4.4 Power consumption and savings

The overall power consumption of the aircraft is driven by the thruster. Its requirement to operate at its given conditions to generate the forward force is either provided by a unique power source in the fully-electric architecture, or from the turbofans in the turbo-electric one. As such, it is important to consider the shaft power demand from the fan $\mathcal{P}_{S,\text{BLI}}$ rather than its available power to generate work $\mathcal{P}_K^*$, as losses are taken into account. In the fully-electric scenario, the power consumption from the turbofan $\mathcal{P}_{\text{pod,PFC}}$ is obtained from an in-house code and is added to the thruster power demand to yield the total power consumption $\mathcal{P}_{\text{PFC}}$ from the PFC. In the turbo-electric thrust-splitting architecture, the power requirement from the aft-mounted thruster drives the power off-take from the main under-wing engines, to which a transmission efficiency η_{trans} is applied. This is done so to approximate losses from the mechanical power extraction from the low-pressure turbine, conversion into electrical power, transport and conversion back to a mechanical supply. This black-box is considered as such as the transmission system sizing and efficiency are out of the scope of this work.

With PFC, there is an opportunity to rescale the under-wing engines to improve further the aero-propulsive performance, as their force generation requirement is reduced. Initially producing half of the propulsive force, each turbofan in the PFC contributes to half of the remaining portion of forward force (1 − PFS). Therefore, the overall power consumption from the PFC is given by $\mathcal{P}_{\text{PFC}}$ which lumps together the power consumption from the podded engines $\mathcal{P}_{\text{pod,PFC}}$ and the power supply to the BLI fan accounting for various transmission efficiencies η_{trans} as given in Eq. (14).

$$\mathcal{P}_{\text{PFC}} = \mathcal{P}_{\text{pod,PFC}} + \mathcal{P}_{\text{BLI}} = \mathcal{P}_{\text{pod,PFC}} + \frac{\mathcal{P}_{S,\text{BLI}}}{\eta_{\text{trans}}} \tag{14}$$

To quantify the savings of the PFC, the power consumption is compared with the reference aircraft, in a similar fashion that the work from Smith Jr. [13]. Smith Jr. introduced a power saving coefficient (PSC) to quantify the reduction in mechanical power from a wake-filling engine relative to a podded one of equivalent areas. However, the reduction in forward force contribution from the under-wing turbofans (intrinsically translated into a reduction in engine size) led to further investigations [42, 43] and subsequent PSC definitions [22, 43, 44] to circumvent the equivalence ambiguities. In this work, the PSC is defined by Eq. (15) by comparing the power requirement from the BLI aircraft with the reference aircraft where savings in power are achieved with positive values.

$$\text{PSC} = 1 - \frac{\mathcal{P}_{\text{PFC}}}{\mathcal{P}_{\text{A/C,ref}}} \tag{15}$$

Although power savings are reported, the metric is a surrogate of fuel burn, as given by Eq. (10). With the assumptions that the same fuels with the same properties are used in both reference and novel aircraft, the PSC reduces to a fuel saving coefficient (FSC) as introduced in Eq. (16). The consideration of future fuels for the PFC predicts to contribute further towards lager FSC, e.g. additional fuel savings of 36% could theoretically be claimed if liquid hydrogen (LH_2) was used similarly to kerosene, and no tanks for storage or heat exchanger for operation were required.

$$\text{FSC} = 1 - \frac{\dot{m}_{f,\text{PFC}}}{\dot{m}_{f,\text{A/C,ref}}} \tag{16}$$

4.5 Application to a propulsive fuselage

The aero-propulsive performance assessment approach is applied to the following PFC. A BLI propulsor is circumferentially integrated around the aircraft tail at 60% of its length ($L_{\text{slope}}/L_{\text{tail}} = 0.60$), which corresponds to a propulsor fan axial location of 90% of the fuselage length.. Its fan ingests around 43% of the mass-flow present in the BL, with its hub radius being a third of the fuselage radius, and applies a pressure ratio of 1.40 with a polytropic efficiency of 90%. At these operating conditions, for a design point at cruise of M0.78 and FL350, the aft-end thruster generates 40.6% of the overall propulsive force requirement (each under-wing engine contributing to 29.7%). The thruster propulsive efficiency κ^* amounts to 72.88%, which is slightly larger than

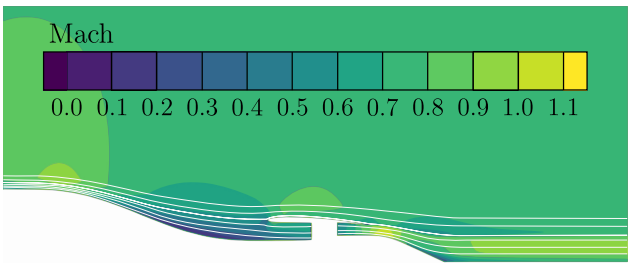


Fig. 11 Mach number contours around a propulsive fuselage concept, with streamlines through the propulsor and over its cowl

typical turbofan propulsive efficiency [1] at an arbitrary position, size and operating point. A representation of the concept is given in Fig. 11 with the Mach contours distribution and streamlines.

5 Power saving coefficient sensitivity to propulsion systems performance

5.1 Influence of under-wing engines in the power saving coefficient calculations

5.1.1 Impact of reference engines in the reference aircraft

As identified by Moirou et al. in Ref. [3], there are large discrepancies in PSC for similar concepts. This is primarily due to the choice made in the reference aircraft, and its reference engines. In PFC scenarios, the comparison with a conventional tube-and-wing aircraft carrying the same number of passengers and operating at the same flight conditions gives the benefits emanating only from BLI, with the most like-to-like comparison. In more disruptive airframes, the comparison is not as easy as the benefits claimed could either be attributed to BLI or to the redesign of the airframe. In these scenarios, the reference aircraft can either be defined equivalent with podded engines, hence showcasing the BLI benefits only, or as a tube-and-wing aircraft and therefore quantifying the synergistic benefits given by the novel architecture. Whilst both references are valid, it is recommended to use a similar airframe in the BLI and non-BLI scenarios to report BLI benefits. If the objective is to quantify the overall benefits offered by the BLI aircraft, including other improvements, then a common reference aircraft can be used.

Focussing on PFC, savings in terms of power ranging from 6 to 15+% [15, 45] are not only attributed to differences in the propulsive performance of the thruster, but also depend on the reference aircraft and engines. As a matter of fact, fuel savings of 15% are already obtained by comparing similar aircraft propelled with two LEAP-1 turbofans versus two CFM56 [46]. This discrepancy is a result of differences in architectures such as the by-pass ratio (11:1 vs 6:1), overall pressure ratio (40 vs 31) and advanced technologies like found in the blades, bleeding, and combustion chamber. To circumvent the first ambiguity associated to the different claims, a consensus needs to be found amongst researchers to have common points of comparison.

5.1.2 Aft-mounted propulsor with retrofit state-of-the-art under-wing turbofans

A first approach is taken by retrofitting the turbofans from the reference aircraft onto the PFC. By doing so, technology levels are set but the engine operates at off-design conditions as less thrust is required, and power is extracted from the shaft to drive the thruster. Whilst there is no minimal bound to the PSC (i.e. the minimum is achieved by mounting inefficient under-wing engines), retrofitting the same engines is the most pragmatic approach to provide conservative savings. For example, considering the PFC introduced above, a PSC of 10.35% is achieved. These savings increase to 16.17% if the reference aircraft is propelled by two CFM56 turbofans, highlighting almost 6% of savings from the change in turbofans.

To understand the reasons of such performance, a savings decomposition is enabled through the simple modelling of the TF with an electric ducted fan. A crude assumption is taken whereby the same output force is generated by the fan within a nacelle (versus the TF). In doing so, component efficiencies are isolated such as the intake, fan and exhaust and the benefits broken-down in Fig. 12. Notably, a *fair* replica of the TF without its core suggests a PSC of 9.50%, attributing 0.85% of the savings to the engine core ((b) in Fig. 12). Similarly, increasing the exhaust efficiency to the technology level envisaged on the thruster attributes 3.22% to the exhaust (c), which compounds to 4.51% when total pressure losses are reduced (d). On the fan, bringing down its pressure ratio from 1.49 to the operating FPR of the thruster (to maintain an equivalent shaft rotational speed), reduced the PSC to 4.40, corresponding to 0.59% of savings attributed to the fan (e). These figures are obtained in the retrofit scenario, meaning that the turbofans mounted on both the reference and PFC aircraft have the same properties. The remaining 4.40% are then the pure consequence of BLI energy harvesting and the nacelle size down-scaling as the mass-flow rate through the engines reduce. However these figures are all obtained when ideal transportation of the power if guaranteed and decreasing this efficiency to 95% reduces the PSC by 1.69%, to 8.66% (a), and to 14.59% (versus 16.17 with CFM56 mounted on the reference aircraft).

5.1.3 Aft-mounted propulsor with re-designed state-of-the-art under-wing turbofans

Large force contributions from the thruster enable a down-scaling of the under-wing engines which inherently decrease their installation aerodynamics penalties and contribute to further benefits. Therefore, there is an opportunity in redesigning the turbofans such that their on-design point is at cruise

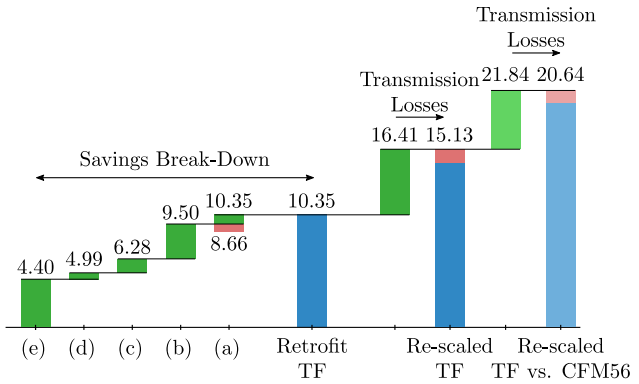


Fig. 12 Power saving coefficient sensitivity to different propulsion system efficiencies

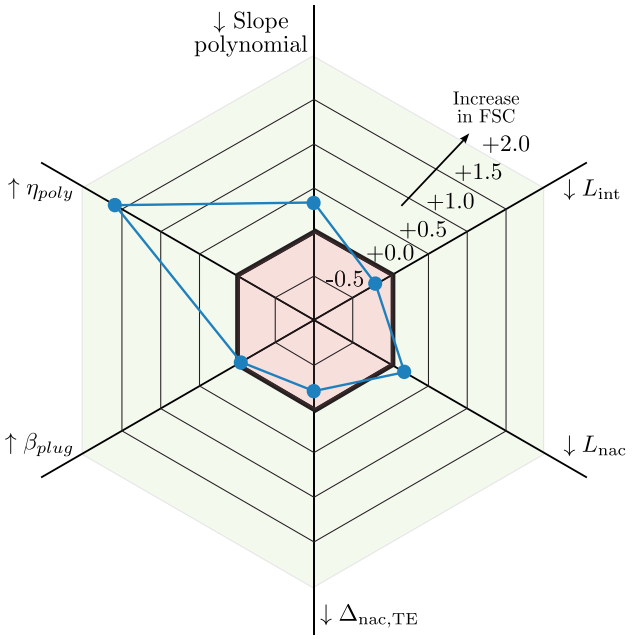


Fig. 13 Sensitivity of the fuel saving coefficient, with gain in green and loss in red, to changes in thruster design variables (rises ↑, or decreases ↓) from the baseline configuration with FSC = 10.5%

for the given force and power off-take combination. In doing so, additional savings of 6.06 and 6.47% are achieved with this particular thruster design (with 100% and 95% transmission efficiencies, respectively). Trading the TF in the reference aircraft with two CFM56, the savings amount to 21.84 and 20.64% respectively with 100 and 95% transmissions efficiencies. The redesign of the TF therefore offers around 6% more in PSC and contribute greatly to the BLI benefits. This clearly demonstrates the ambiguity that stands in the definitions of the under-wing engines in both reference and propulsive fuselage aircraft as PSC between 4.4 and 21.8% can be claimed. It becomes rather important in these scenarios to describe the engine models to compare concepts between them.

5.2 Impact of the aft-thruster design and performance

5.2.1 Influence of the thruster design

It has been shown that for a given BLI propulsor design and performance, PSC is very sensitive to the under-wing engine models. However, PSC is mainly driven by the thruster design and performance as it harvests the energy present in the BL flow, and enables further savings from the under-wing turbofans by re-scaling them. To try and appreciate the influence the thruster design has on the vehicle performance and the fuel savings, Fig. 13 gathers the relative difference in FSC between the designs and the initial design considered previously, with retrofit turbofans (with variations in parameters reported on the axes).

It is observed that mild benefits are achievable by changing the polynomial order of the Bell-Mehta curve (with a slender slope, alike in Ref. [21]), shortening the nacelle or reducing the plug angle, with *only* 0.5% additional benefits. However, it is pre-empted that these design parameters can have detrimental effects on the performance as sharp accelerations, or flow separation can be expected on these wall surfaces. This highlights that several intensity (or sensitivity) levels are observed, as given by the throat area, fan polytropic efficiency, η_{poly}, or the polynomial order of the Bell-Mehta curve defining the pre-diffusive slope. For instance, improving the polytropic efficiency of the fan by 5% raises the PSC by 1.6%. Conversely, an increase in fan pressure ratio from 1.4 to 1.6 reduces the PSC by 3.4%, and ingesting a larger amount of mass-flow present in the BL showcases penalties of 3.03% (relative to the reference aircraft). It is hypothesised that primary effects on the performance and savings are observed with changes in mass-flow and pressure rise, and secondary effects with changes in the propulsor shape, for a given position of the propulsor along the aircraft tail.

5.2.2 Influence of the thruster efficiency

Greater fuel savings are achieved with improved BLI propulsor performance. In the previous discussions, the thruster fan featured an initial fan polytropic efficiency of 90%, which is brought to 93 and 95% respectively to represent potential future technology improvements. Consequently, improvements in PSC of 1.04 and 1.63% are achieved for the same net axial force, using the retrofit engines. These savings are primarily due to less additional

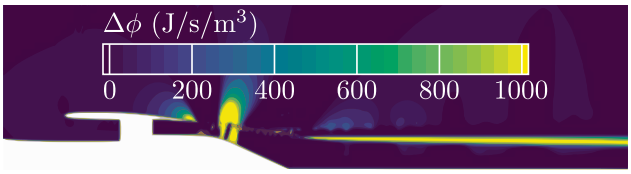


Fig. 14 Difference in local volume-specific viscous dissipation rate for fan polytropic efficiencies of 90% and 95% on the baseline thruster

power to apply the same pressure rise as a similar amount of energy is harvested by the fan from the flow, and a larger conversion rate is enabled.

Denton demonstrated that loss generations in turbomachinery are measured by entropy production [47]. However, this work did not distinguish reversible and irreversible entropy production that is attributed to irreversible heat transfers within the fluid and to viscous dissipation as identified by Refs. [48, 49]. Theses losses are defined as the irreversible entropy generation rate per unit volume in Ref. [48]:

$$\theta = \frac{\overbrace{\left(\overline{\overline{\tau}} \cdot \nabla\right) \cdot \boldsymbol{V}}^{\phi}}{T} + \frac{\boldsymbol{q} \cdot \boldsymbol{q}}{k_t T^2} \tag{17}$$

Whilst these losses are contained within the exergy balance as the total energy production (or exergy destruction) [11], the energy-based balance omits thermal effects to only consider mechanical energy transfers. Therefore, Fig. 14 illustrates the changes in local volume-specific viscous dissipation rate production ϕ behind the fan of $\eta_{\text{poly}} = 90\%$ and 95% scenarios. Notably, the higher propulsive efficiency reduces losses in the jet/wake mixing regions and contributes to a better utilisation of the energy present in the flow. The larger fan polytropic efficiency leads to a rise in propulsive efficiency κ^* from 72.88 to 80.56%. This results from a reduction in electric power demand from 4.21 to 3.94 MW (a 9.4% reduction) from the thruster's fan. Subsequently, the jet dissipative effects, Φ_{JET} are reduced by 4%.[2] However, relative to the power addition in the flow, as given by $\mathcal{P}_{S,\text{BLI}}$, the thruster with higher polytropic efficiency dissipates more relative to the baseline. In other terms, the jet dissipates 9.29% of the energy provided by the fan ($\Phi_{\text{JET}}/\mathcal{P}_{S,\text{BLI}} = 9.29\%$), in the baseline configuration, whereas 9.55% is dissipated for the larger polytropic efficiency.

[2] The jet-plume viscous dissipation rate is computed following the precedence procedure detailed in Ref. [26], where the different flow features are identified and decomposed.

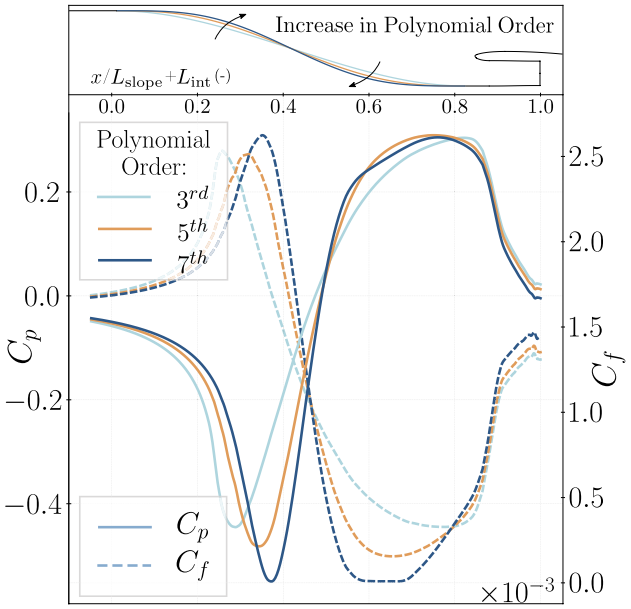


Fig. 15 Local pressure and skin-friction coefficients distribution along the pre-diffusive slope for different curve polynomial orders

5.2.3 Influence of the slope design in the thruster performance

In addition to the propulsor performance impact on the savings, the impact of the pre-diffusive slope on its surroundings is investigated with the local pressure coefficient C_p and skin-friction coefficient C_f distributions. Three Bell-Mehta polynomial orders are represented in Fig. 15. Notably, a higher order prevents initial abrupt changes in velocity as noted with a larger C_f just behind the change in curvature point. However, the higher order favours a larger steepness at mid-curve with a large negative C_p followed by an abrupt change in positive C_p where a flow detachment upstream of the nacelle is observed. This is confirmed by C_f where no skin-friction is noted along this portion of the surface. In these cases, flow recirculation increases the drag of the aircraft that needs to be overcome by the propulsion systems to maintain steady-level flight and consume more fuel, reducing κ^* from 72.88 to 71.63%.

5.3 Propulsive fuselage concept aircraft with an ideal under-wing propulsion system

To circumvent the definition of the under-wing engines, they are fully idealised with propulsive efficiencies of 100%. These are unrealistic as the device size will be close to infinite to reduce the jet velocity and losses in the plume but their idealisation defines the maximal bound of PSC achievable by a BLI thruster design. Assuming a given PFS is ensured in the PFC, the remaining force requirement is

obtained when only requiring the remaining force power to operate. The savings that would be achieved in that scenario are therefore represented with the potential power saving coefficient (PPSC) given by Eq. (18) as a special case of Eqs. (15) and (16).

$$\mathrm{PPSC} = 1 - \frac{\mathcal{P}_{\mathrm{BLI}} + (1 - \mathrm{PFS})\mathcal{F}_{\mathrm{PFC}} \cdot V_{\mathrm{B}}}{\mathcal{P}_{\mathrm{A/C,ref}}} \tag{18}$$

In the example taken earlier, the PPSC amounts to 61.32% with ideal transmission efficiency, and 60.39% when reduced to 95%. Despite providing any tangible interpretation, as unachievable,[3] the metric principal strength is its universality. When considering an ideal propulsion system to generate a forward force, a fair and unique comparison is enabled between different aircraft concepts to only evaluate the performance of the aft-mounted propulsor, and hence its sole BLI benefits. Its universality allows one to consider turbo- or fully-electric aircraft architecture whereby a unique power source would provide energy to all propulsion systems. Although absolute values of PSC's are rather insignificant, a quantification of the improvements is granted by changes in the thruster design, or propulsive performance. Nonetheless, one should be careful and not optimise aircraft with this as an objective function as the optimiser will try to reduce the PFS and make the ideal propulsion system provide all propulsive force necessary.

A step further towards mitigating all challenges related to the definition of the on-board engines consists in comparing the PFC with a reference aircraft itself propelled with an ideal propulsive source. In this scenario, the savings are given by Eq. (19), as an extension to the definition given in Ref. [12] not considering thrust-splitting aircraft architectures. Nonetheless, positive PSC values are only expected when the thruster, in the PFC, outperforms the ideal propulsion systems. In these cases, pure BLI benefits are highlighted showcasing the energy recuperation by the fan from the viscous flow. The main strength of this metric is therefore to represent the achieved savings by comparing different BLI propulsor designs and propulsive performances. Notably, retrieving the previous examples, the *minimum*[4] PSC is −9.12% with ideal transmission versus −11.74% with a 95% transmission efficiency.

$$\mathrm{PSC}_{\mathrm{min}} = 1 - \frac{\mathcal{P}_{\mathrm{BLI}} + (1 - \mathrm{PFS})\mathcal{F}_{\mathrm{PFC}} \cdot V_{\mathrm{B}}}{\mathcal{F}_{\mathrm{A/C,ref}} \cdot V_{\mathrm{B}}} \tag{19}$$

5.4 Propulsive fuselage concept aircraft with ideal under-wing and aft-mounted propulsion systems

The maximal energy harvesting is achieved when an hypothetical ideal BLI propulsor is integrated to the aircraft. To estimate these benefits, the clean morphed fuselage is used to compute the irreversible losses at the vehicle trailing edge and define a potential for energy recovery (PER) [9, 12]. This definition relates back to the energy-based balances between the power sources and sinks within a unique control volume of an unpowered configuration whereby the theoretical maximum recoverable energy is defined. Nonetheless, it differs from Ref. [9] whose only involves the viscous dissipation rate and over-predicts the real potential recovery, and Ref. [12] whose accounts for all compressibility effects, and does not decompose the reversible and irreversible components, but accounts for the residual losses.

Generically, PER is better defined by taking an exergy standpoint to dissociate the mechanical and thermal exergy rates, and their recoverable (energy/exergy) and irrecoverable (energy) components. However, in adiabatic investigations (no heat added to the system), a corrected energy-based definition of PER is given by Eq. (20) accounting for the viscous dissipation rate at the trailing edge Φ_{TE} (which can be corrected from an exergy point of view as the viscous dissipation represents a loss in mechanical energy but a gain in thermal exergy [11]) and the rate of irrecoverable volumetric pressure work $\Theta_{\mathrm{irr,TE}}$. Even though Φ is composed of an irrecoverable part dissipated as heat and another that could be recovered from an heat exchanger, this is outside the scope of this study. Similarly, Θ contains an irrecoverable component of the rate of volumetric pressure work from compressible effects represented with Θ_{irr} and a recoverable component that cancels out further downstream in the aircraft wake.

$$\mathrm{PER}_{\mathrm{cc}} = 1 - \frac{\Phi_{\mathrm{TE}} + \Theta_{\mathrm{irr,TE}}}{\mathcal{F}_{\mathrm{fus,MOR}} \cdot V_{\mathrm{B}}} \tag{20}$$

Overall, the quantity $\mathrm{PER}_{\mathrm{cc}}$, accounting for the compressibility correction, is interpreted as the maximal power benefit achievable by using an unducted BLI thruster that ingests the entire viscous layer and perfectly fills its energy defect without interfering with the flow-field upstream and around. This echoes $\mathrm{PSC}_{\mathrm{min}}$ where integration losses are considered but does not represent either a practical maximum as PSC beyond this value can be achieved when the free-stream ingesting ideal propulsion system is traded for engines,

[3] There would be no need for BLI if ideal propulsive efficiency could be achieved by under-wing turbofans.

[4] There is a caveat in the use of the word "minimum" as it considers unrealistic ideal scenarios. However, consistency is kept in the naming convention with Ref. [12] which considers non-thrust-splitting aircraft.

hence lowering the performance of the reference aircraft and showcasing the benefits of ingesting the developed boundary layer flow. However, the metric attracts one attention at preliminary design stages when shaping the fuselage, or airframe, to gauge the potential savings the vehicle offers. Similar to the other PSC metrics defined in powered aircraft, PER_{cc} values can be compared between designs to evaluate the potential gains the different airframe shapes could offer. For reference on the morphed baseline considered earlier, PER_{cc} is evaluated at 11.4%.

Lastly, recent efforts in decomposition methods allow one to track the potential for energy recovery along bodies. In the definition of Eq. (20), this is not possible as the denominator corresponds to the fuselage drag and is not breakable. However, when considering velocity decomposition methods as given in Ref. [50], and partial pressure field in Ref. [51], their unification performed by Mutangara et al. in Ref. [52] allows to track all reversible and non-recoverable components of the power balance terms and therefore quantify the PER at any given position. An advantage of such methods is to quantify the potential for energy harvesting at the fictitious position of the BLI propulsor and therefore pre-morph the aircraft tail before the propulsor integration.

5.5 Universality of the metrics

The three metrics introduced (PPSC, PSC_{min} and PER_{cc}) have all been applied to a PFC, however they are equally applicable to other concepts. The comparison with ideal propulsion systems removes all kind of ambiguities associated with the performance of the reference propulsion system, as well as the conservation of the same airframe between BLI and non-BLI scenarios. For example, the MIT D8 claims power savings of 7–10.5% [22, 23] which are the pure result of BLI benefits (comparison of the lifting airframe with podded engines versus embedded engines), but reports fuel savings of 36% purely based on changes in configuration (lifting fuselage versus tube-and-wing), which could compound to 65–71% with technologies advancements in 20–30 years [23]. Similarly on the NASA N3-X, fuel savings of more than 70% are expected when comparing the concept to a Boeing 777-200LR [53]. These figures could appear as very optimistic but are mainly based on the point of comparison, and the assumptions made on the synergies and their contributions to the fuel savings.

In the examples given, PER_{cc} becomes essential to pre-evaluate the potential savings the airframe offers. In these lifting fuselages, crude assumptions can be taken whereby the fuselage upper surface is assimilated to a flat plate and where it is known to yield potential recuperation of 8–15% of the energy imparted to the flow (as a function of the Reynolds number) [12]. For better estimates, CFD on the airframe can be performed and PER evaluated at any given position. The main advantage arises from PSC_{min} where the reference airframe is propelled by ideal propulsion systems to generate the remaining thrust required. The metric can be used to evaluate the performance of the integrated engines where their positions, numbers or shapes can be changed. Additionally, when idealising the BLI propulsion system in such a way that it only fills the defects in momentum, or by analogy harvest the energy present in the flow, the metrics tend towards PER_{cc} where the delta in values attributes the losses to integration penalties (of the duct(s)).

6 Conclusion

In this work, a novel performance evaluation framework for aircraft incorporating boundary layer ingestion (BLI) is developed to assess preliminary design-level aero-propulsive performance. The aircraft model is simplified to 2D axisymmetric studies to demonstrate the new approach, building on established momentum- and energy-based methods whilst introducing new metrics. Unlike previous studies, which applied momentum-based schemes to complex geometries or energy-based methods to simplified cases, this work bridges the gap by applying the methodology to propulsive fuselage concepts. A key strength of this approach is the simplification of wing-body aircraft to a fuselage and propulsor assembly to advise on preliminary overall vehicle performance.

The power balance is corrected in this work by refining the existing $\mathcal{P}_K$ term, which represents the additional power imparted by moving surfaces, such as fan blades. This correction isolates the power available to do work on the fluid, distinguishing it from total power input by identifying inherent losses within the propulsor, including viscous dissipation and irrecoverable pressure work. Whilst the numerator for useful work remains for future refinement, this correction brings the definition of propulsive efficiency closer to accuracy, which is critical for evaluating vehicle performance and fuel savings.

Power or fuel savings are often used as key metrics to compare novel aircraft configurations to conventional ones, aligning them with aviation's environmental goals. However, the power saving coefficient (PSC) has been a source of controversy due to its definition, assumptions, and choice of reference aircraft and engines. To resolve these ambiguities, this work introduces new metrics that bound the practical minimum (PSC_{min}) and potential maximum values (PPSC)

of PSC. For clean fuselages, the potential for energy recovery (PER) is corrected to account for compressibility effects (PER_{cc}) and its non-recoverable portion.

Future work should include the development of a body-force model to replace the boundary conditions that represent the propulsion system to validate κ^*, as well as the extension to three-dimensional studies with wing-body propulsive fuselage aircraft. Whilst this work provides new metrics to evaluate the potential performance of future concepts, more realistic figures will be obtained with the proposed further developments.

Appendix 1: Coupled domain size and grid refinement study

A grid dependence study is conducted following Celik et al.'s procedure alongside a domain size study [39]. On the reference fuselage, precedence is given to fine boundary layer and wake regions to accurately capture the net stream-wise force from *near-field* and *far-field* computations. To ensure the boundary conditions do not interfere with the flow-field around the fuselage, the domain size is varied in three fashions that extend further downstream the body. As such, the domain and control volume for analysis follow Fig. 8 whereby $d_{FS} = 10\,L_{fus}$ and $d_{TP} = 20\,L_{fus}$. To evaluate the sensitivity of the solution to the presence of the outlet boundary condition at the Trefftz plane, three domain sizes are investigated: $d_{outlet} = 20\,L_{fus}$, $d_{outlet} = 30\,L_{fus}$ and $d_{outlet} = 40\,L_{fus}$, respectively representing the small, medium and large domains.

The *near-field* force $\mathcal{F}_{fus,nf}$ is computed following Eq. (9) whereas the *far-field* one $\mathcal{F}_{fus,ff}$ is computed from Eq. (7), where both variables are respectively identified as ϕ_1 and ϕ_2 in Table 1. Lastly, their relative difference is also represented and identified as ϕ_3 in Table 1 and used to monitor convergence. The thresholds to trigger convergence are all residuals below 10^{-6} and $\phi_3 < 0.5\%$. Table 1 summarises the coupled grid and domain convergence study that follows Ref. [39] conventions whereby the following is considered: the number of cells N, grid size h and key variables ϕ_i. In addition, the comparison between the coarse and medium mesh (Coar./Med.), and medium and fine mesh (Med./Fine) is given with the following: the refinement factor r, variable error ϵ, apparent order p, extrapolated variable ϕ^{ext}, its approximate error e^a, its extrapolated error e^{ext} and the grid convergence index GCI. Additionally, the error range is provided with its minimum and maximum bounds on the extrapolated variables. A very close agreement in forces is obtained from the *near-field* force and *far-field* energy formulations, which is within 0.01, −0.27, and −0.31% for the coarse, medium and fine grids, respectively, with the larger domain. Furthermore, the numerical uncertainty in the fine grid solution is less than 0.6% for all domain sizes, based on the GCI definition.

Appendix 2: Force convergence comparison

The net stream-wise force is evaluated from *near-field* integration as previously mentioned, as well as in the *far-field* by sweeping different transverse plane at each fuselage chord behind the body until d_{TP} at twenty fuselage lengths behind is reached. This allows to track the convergence of the far-field force from an energy standpoint relative to the *near-field* force, from skin-friction and pressure forces. The spatial convergence is given in Fig. 16 where it is observed a good prediction of the total net stream-wise force for all grids just behind the fuselage on the larger domain, especially for the finest two meshes. This convergence advises that, on the larger domain size, the medium mesh size can be down-selected for the next investigations as it provides a good agreement (error smaller than 0.1%) with a mesh more than three times denser (around 0.53 million cells versus 1.85 millions cells).

Appendix 3: Aircraft drag build-up

To relate the CFD solution of the bare fuselage to the entire aircraft drag, a drag build-up method is followed from Refs. [28, 29]. In this approach, available data from short-to-medium range aircraft are retrieved and mapped out under different flight Mach numbers at a flight-level of 35,000 ft above the sea level. Figure 17 summarises the correlation between the lift coefficient and the lift-to-drag ratio (L/D) to relate it to an overall drag coefficient broken-down into its profile, induced and wave drag components. Notably for the aircraft considered, a L/D of 19 advises on $C_L = 0.6$ (top-left corner) which corresponds to a 54.4% lift-independent C_{D_0}, 41.8% lift-induced C_{D_i}, 2.2% wave drag C_{D_w}, and 1.6% of trim drag (not represented here). Of these 54.4%, the different aircraft components aerodynamically decoupled are computed (bottom-right corner) and their shares given with: 7.9% for the nacelles, 12.9% for the empennage assembly (vertical and horizontal stabilisers), 34.2% for the wings and 45% for the bare fuselage. Overall, this represents a share drag of 24.5% of the overall aircraft drag that is attributed to the fuselage (as the non-lifting fuselage is assumed to not have any lift-induced and wave drag), permitting the estimation of the overall aircraft drag from CFD by just computing the bare fuselage.

Table 1 Domain and size convergence study on three grid and three domain sizes

Domain	Small			Medium			Large		
Mesh	Coarse	Medium	Fine	Coarse	Medium	Fine	Coarse	Medium	Fine
N	56356	517096	1815516	64848	525398	1834598	73533	528363	1855043
h	3.156	1.042	0.556	3.420	1.201	0.643	3.605	1.345	0.718
ϕ_1 (N)	9129.49	9125.07	9126.57	9129.33	9124.92	9122.10	9129.14	9124.76	9126.28
ϕ_2 (N)	9104.78	9081.17	9079.25	9120.38	9093.67	9084.95	9130.30	9100.58	9098.09
ϕ_3 (%)	− 0.271	− 0.481	− 0.519	− 0.098	− 0.342	− 0.407	0.013	− 0.265	− 0.309

Domain	Small		Medium		Large	
Mesh	Coar./Med	Med./Fine	Coar./Med	Med./Fine	Coar./Med	Med./Fine
r	3.029	1.874	2.846	1.869	2.681	1.874
ε_1 (N)	− 4.42	1.5	− 4.412	− 2.827	− 4.379	1.515
ε_2 (N)	− 23.607	− 1.923	− 26.712	− 8.73	− 29.721	− 2.489
ε_3 (%)	− 0.210	− 0.038	− 0.244	− 0.065	− 0.278	− 0.044
p_1	–	0.759	–	0.083	–	0.866
p_2	–	1.391	–	0.475	–	1.683
p_3	–	0.829	–	0.634	–	1.166
ϕ_1^{ext} (N)	9132.84	9122.62	9177.74	9177.74	9132.39	9122.66
ϕ_2^{ext} (N)	9111.21	9082.55	9161.89	9118.92	9137.28	9101.90
e_1^a (%)	0.05	0.02	0.05	0.03	0.05	0.02
e_2^a (%)	0.26	0.02	0.29	0.10	0.33	0.03
e_1^{ext} (%)	0.04	0.03	0.53	0.58	0.04	0.02
e_2^{ext} (%)	0.07	0.02	0.45	0.28	0.08	0.02
GCI_1 (%)	0.03	0.02	0.11	0.13	0.03	0.02
GCI_2 (%)	0.09	0.01	0.57	0.13	0.10	0.01
ϕ_1^{min} (N)	9130.00	9120.16	9167.85	9124.93	9129.49	9120.57
ϕ_1^{max} (N)	9135.68	9125.07	9187.63	9230.56	9135.28	9124.76
ϕ_2^{min} (N)	9103.17	9081.17	9109.78	9093.68	9128.55	9100.58
ϕ_2^{max} (N)	9119.26	9083.93	9214.01	9144.17	9146.02	9103.23

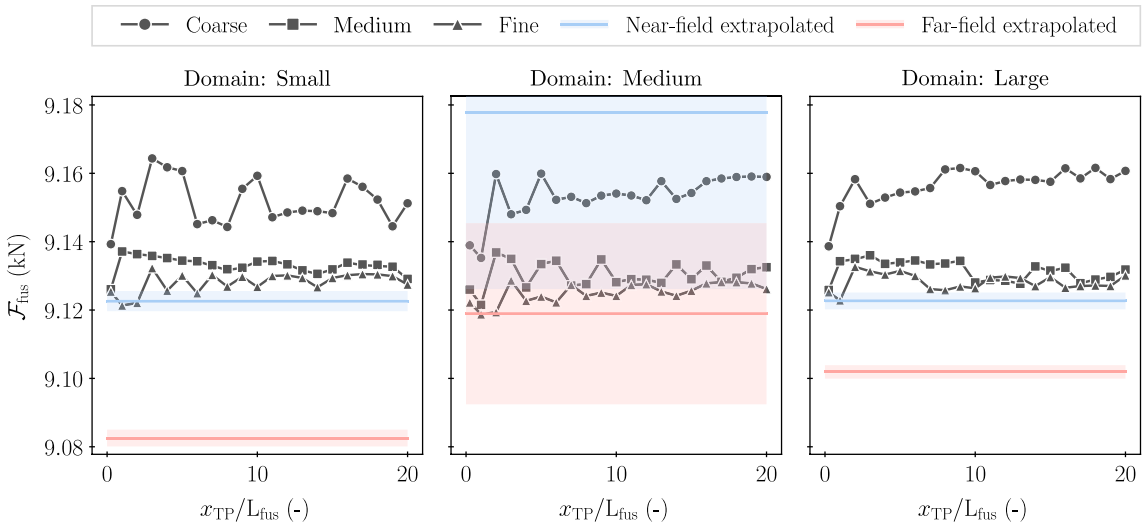


Fig. 16 Comparison of net stream-wise force between the *near-field* and *far-field*, as computed, and their extrapolated values from the Table 1

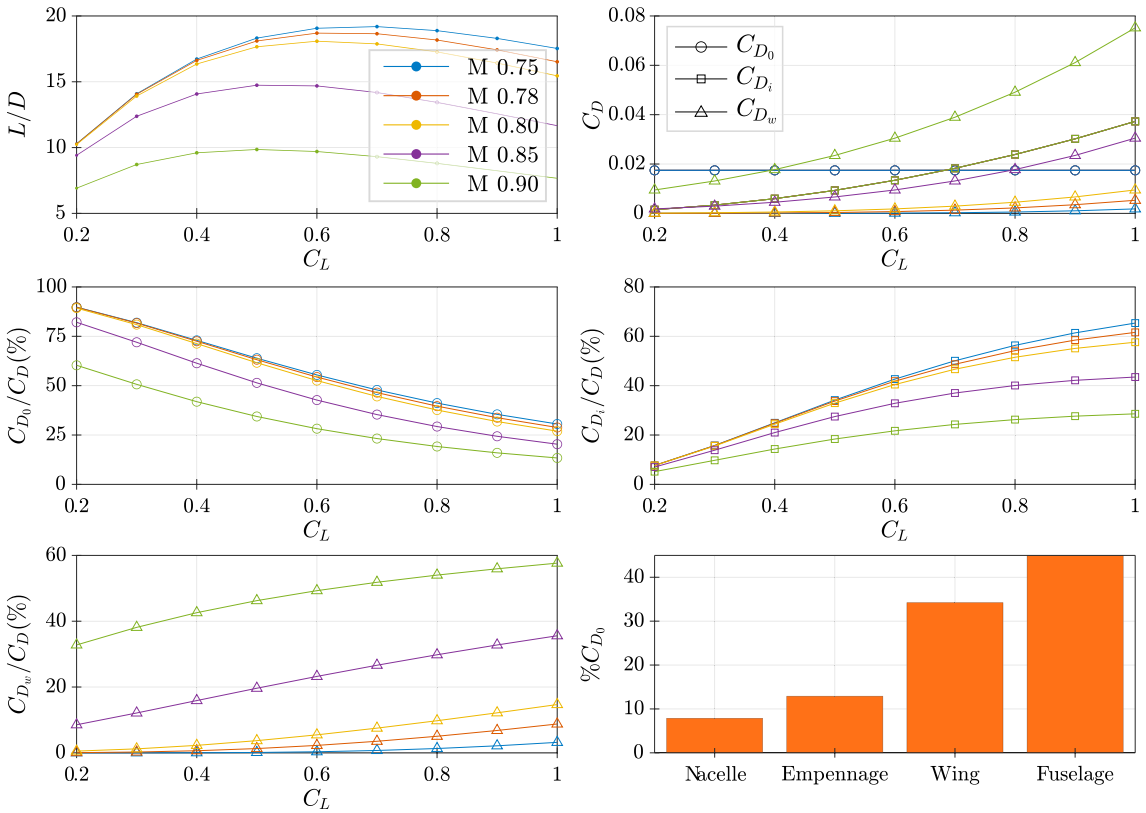


Fig. 17 Drag build-up of the reference aircraft, for an assumed lift-to-drag ratio $L/D = 19.0$ at M_{B} 0.78, corresponding to a lift coefficient of $C_L = 0.6$

Acknowledgements This work was conducted within the SUBLIME (Supporting Understanding of Boundary-Layer Ingestion Model Experiment) project as part of the Clean Sky 2 Joint Undertaking which has received funding from the European Union's Horizon 2020 research and innovation programme under Grant Agreement No. 864803. The authors express their gratitude to Panagiotis Giannakakis from Safran S.A. for the fruitful discussion on the power savings decomposition.

Author contributions Nicolas G.M. Moirou: conceptualisation, data curation, investigation, methodology, software, visualisation, writing—original draft, writing—review & editing. Drewan S. Sanders: project administration, supervision, validation, writing—review and editing.

Data availability No datasets were generated or analysed during the current study.

Declarations

Conflict of interest The authors have no conflict of interest to declare that are relevant to the content of this article.

Open Access This article is licensed under a Creative Commons Attribution 4.0 International License, which permits use, sharing, adaptation, distribution and reproduction in any medium or format, as long as you give appropriate credit to the original author(s) and the source, provide a link to the Creative Commons licence, and indicate if changes were made. The images or other third party material in this article are included in the article's Creative Commons licence, unless indicated otherwise in a credit line to the material. If material is not included in the article's Creative Commons licence and your intended use is not permitted by statutory regulation or exceeds the permitted use, you will need to obtain permission directly from the copyright holder. To view a copy of this licence, visit http://creativecommons.org/licenses/by/4.0/.

References

1. Epstein, A.H.: Aeropropulsion for commercial aviation in the twenty-first century and research directions needed. AIAA J. **52**(5), 901–911 (2013). https://doi.org/10.2514/1.J052713
2. Okonkwo, P., Smith, H.: Review of evolving trends in blended wing body aircraft design. Prog. Aerosp. Sci. **82**, 1–23 (2016). https://doi.org/10.1016/J.PAEROSCI.2015.12.002
3. Moirou, N.G.M., Sanders, D.S., Laskaridis, P.: Advancements and prospects of boundary layer ingestion propulsion concepts. Prog. Aerosp. Sci. **138**, 100897 (2023). https://doi.org/10.1016/j.paerosci.2023.100897
4. MIDAP Study Group: Guide to in-flight thrust measurement of turbojets and fan engines. Tech. Rep. AGARD-AG-237 (1979)
5. E-33 In Flight Propulsion Measurement Committee: In-flight thrust determination. Tech. Rep. AIR1703 (1985). https://doi.org/10.4271/AIR1703A
6. Sanders, D.S.: Boundary layer ingestion performance assessments with application to business jets. Ph.D. thesis, Cranfield University, Cranfield, United Kingdom (2018)
7. Habermann, A.L., Bijewitz, J., Seitz, A., Hornung, M.: Performance bookkeeping for aircraft configurations with fuselage wake-filling propulsion integration. CEAS Aeronaut. J. **11**, 529–551 (2019). https://doi.org/10.1007/s13272-019-00434-w
8. Matesanz-García, J.: Propulsion integration design and evaluation for novel aircraft configurations. Ph.D. thesis, Cranfield University, Cranfield, United Kingdom (2022)
9. Sanders, D.S., Laskaridis, P.: Full-aircraft energy-based force decomposition applied to boundary-layer ingestion. AIAA J. **58**(10), 4357–4373 (2020). https://doi.org/10.2514/1.J058695
10. Drela, M.: Power balance in aerodynamic flows. AIAA J. **47**(7), 1761–1771 (2009). https://doi.org/10.2514/1.42409
11. Arntz, A., Atinault, O., Merlen, A.: Exergy-based formulation for aircraft aeropropulsive performance assessment: theoretical development. AIAA J. **53**(6), 1627–1639 (2015). https://doi.org/10.2514/1.J053467
12. Lamprakis, I., Sanders, D.S., Laskaridis, P.: Fundamental concepts of boundary layer ingestion propulsion. J. Aircr. (under review) (2023)
13. Smith, L.H., Jr.: Wake ingestion propulsion benefit. J. Propul. Power **9**(1), 74–82 (1993). https://doi.org/10.2514/3.11487
14. Gray, J.S., Martins, J.: Coupled aeropropulsive design optimisation of a boundary-layer ingestion propulsor. Aeronaut. J. **123**(1259), 121–137 (2019). https://doi.org/10.1017/aer.2018.120
15. Yildirim, A., Gray, J.S., Mader, C.A., Martins, J.: Boundary-layer ingestion benefit for the STARC-ABL concept. J. Aircr. **59**(4), 896–911 (2022). https://doi.org/10.2514/1.C036103
16. Sanders, D.S.: Aircraft aerodynamic work-energy relationships with mass source considerations. Tech. Rep. RP0028, Cranfield University, Cranfield, United Kingdom (2023)
17. Renard, N., Deck, S.: A theoretical decomposition of mean skin friction generation into physical phenomena across the boundary layer. J. Fluid Mech. **790**, 339–367 (2016). https://doi.org/10.1017/JFM.2016.12
18. Matesanz-García, J., Piovesan, T., MacManus, D.G.: Aerodynamic optimization of the exhaust system of an aft-mounted boundary layer ingestion propulsor. Int. J. Numer. Methods Heat Fluid Flow **33**, 4 (2022). https://doi.org/10.1108/HFF-06-2022-0362
19. Gray, J.S.: Design optimization of a boundary layer ingestion propulsor using a coupled aeropropulsive model. Ph.D. thesis, University of Michigan, Ann Arbor, MI, USA (2018)
20. Habermann, A.L., Gokhale, A., Hornung, M.: Numerical investigation of the effects of fuselage upsweep in a propulsive fuselage concept. CEAS Aeronaut. J. **12**, 173–189 (2021). https://doi.org/10.1007/s13272-020-00487-2
21. Gray, J.S., Mader, C.A., Kenway, G.K., Martins, J.: Modeling boundary layer ingestion using a coupled aeropropulsive analysis. J. Aircr. **55**(3), 1191–1199 (2018). https://doi.org/10.2514/1.C034601
22. Uranga, A., Drela, M., Hall, D.K., Greitzer, E.M.: Analysis of the aerodynamic benefit from boundary layer ingestion for transport aircraft. AIAA J. **56**(11), 4271–4281 (2018). https://doi.org/10.2514/1.J056781
23. Uranga, A., Drela, M., Greitzer, E.M., Hall, D.K., Titchener, N.A., Lieu, M.K., Siu, N.M., Casses, C., Huang, A.C., Gatlin, G.M., Hannon, J.A.: Boundary layer ingestion benefit of the D8 transport aircraft. AIAA J. **55**(11), 3693–3708 (2017). https://doi.org/10.2514/1.J055755
24. Hall, D.K., Huang, A.C., Uranga, A., Greitzer, E.M., Drela, M., Sato, S.: Boundary layer ingestion propulsion benefit for transport aircraft. J. Propul. Power **33**(5), 1118–1129 (2017). https://doi.org/10.2514/1.B36321
25. Sato, S.: The power balance method for aerodynamic performance assessment. Ph.D. thesis, Massachusetts Institute of Technology, Boston, MA, USA (2012)
26. Moirou, N.G.M.: Aero-propulsive performance assessment approach to boundary layer ingestion aircraft. Ph.D. thesis, Cranfield University, Cranfield, United Kingdom (2023)
27. Moirou, N.G.M., Mutangara, N.E., Sanders, D.S.: Fundamental considerations in the design and performance assessment of propulsive fuselage aircraft concepts. Aeronaut. J. **129**, 762–787 (2024). https://doi.org/10.1017/aer.2024.124
28. Gur, O., Mason, W.H., Schetz, J.A.: Full-configuration drag estimation. J. Aircr. **47**(4), 1356–1367 (2010). https://doi.org/10.2514/1.47557
29. Mason, W.H.: Analytic models for technology integration in aircraft design. In: Aircraft Design, Systems and Operations Conference, AIAA 1990-3262, Dayton, OH, USA (1990). https://doi.org/10.2514/6.1990-3262
30. Zhao, X., Yao, H.: BLI turbofan performance maps. Tech. Rep. RP0019, Chalmers University of Technology, Gothenburg, Sweden (2022)

31. Heidebrecht, A., MacManus, D.G.: Surrogate model of complex non-linear data for preliminary nacelle design. Aerosp. Sci. Technol. **84**, 399–411 (2019). https://doi.org/10.1016/j.ast.2018.08.020
32. Kenway, G.K., Kiris, C.: Aerodynamic shape optimization of the STARC-ABL concept for minimal inlet distortion. In: AIAA/ASCE/AHS/ASC Structures, Structural Dynamics, and Materials Conference: AIAA 2018-1912. Kissimmee, FL, USA (2018). https://doi.org/10.2514/6.2018-1912
33. Bell, J.H., Mehta, R.D.: Contraction design for small low-speed wind tunnels. Tech. Rep. CR-177488, Stanford University (1988)
34. Christie, R., Heidebrecht, A., MacManus, D.G.: An automated approach to nacelle parameterization using intuitive class shape transformation curves. J. Eng. Gas Turbines Power **139**(6), 062601 (2017). https://doi.org/10.1115/1.4035283
35. Christie, R., Robinson, M., Tejero, F., MacManus, D.G.: The use of hybrid intuitive class shape transformation curves in aerodynamic design. Aerosp. Sci. Technol. **95**, 105473 (2019). https://doi.org/10.1016/j.ast.2019.105473
36. Tejero, F., MacManus, D.G., Sheaf, C.: Surrogate-based aerodynamic optimisation of compact nacelle aero-engines. Aerosp. Sci. Technol. **93**, 105207 (2019). https://doi.org/10.1016/j.ast.2019.05.059
37. Tejero, F., Christie, R., MacManus, D.G., Sheaf, C.: Non-axisymmetric aero-engine nacelle design by surrogate-based methods. Aerosp. Sci. Technol. **117**, 106890 (2021). https://doi.org/10.1016/j.ast.2021.106890
38. Ansys®ICEM CFD Release 20.2. ANSYS, Inc. (2020)
39. Celik, I.B., Ghia, U., Roache, P.J., Freitas, C.J., Coleman, H., Raad, P.E.: Procedure for estimation and reporting of uncertainty due to discretization in CFD applications. J. Fluids Eng. **130**(7), 078001 (2008). https://doi.org/10.1115/1.2960953
40. Ansys®Fluent Release 20.2. ANSYS, Inc. (2020)
41. Menter, F.R.: Two-equation eddy-viscosity turbulence models for engineering applications. AIAA J. **32**(8), 1598–1605 (1994). https://doi.org/10.2514/3.12149
42. Liu, C., Ihiabe, D., Laskaridis, P., Singh, R.: A preliminary method to estimate impacts of inlet flow distortion on boundary layer ingesting propulsion system design point performance. Proc. Inst. Mech. Eng. Part G J. Aerosp. Eng. **228**(9), 1528–1539 (2014). https://doi.org/10.1177/0954410013496750
43. Giannakakis, P., Pornet, C., Turnbull, A.: Turbo-electric propulsive fuselage aircraft BLI benefits: a design space exploration using an analytical method. Aeronaut. J. **124**(1280), 1523–1544 (2020). https://doi.org/10.1017/AER.2020.26
44. Baskaran, P., Della Corte, B., van Sluis, M., Gangoli Rao, A.: Aeropropulsive performance analysis of axisymmetric fuselage bodies for boundary-layer ingestion applications. AIAA J. **60**(3), 1592–1611 (2022). https://doi.org/10.2514/1.J060362
45. Seitz, A., Habermann, A.L., van Sluis, M.: Optimality considerations for propulsive fuselage power savings. Proc. Inst. Mech. Eng. Part G J. Aerosp. Eng. **235**(1), 22–39 (2020). https://doi.org/10.1177/0954410020916319
46. CFM International: The LEAP engine. https://www.cfmaeroengines.com/engines/leap/ (2023). Retrieved 16 Apr 2023
47. Denton, J.D.: The 1993 IGTI scholar lecture: loss mechanisms in turbomachines. J. Turbomach. **115**(4), 621–656 (1993). https://doi.org/10.1115/1.2929299
48. Wheeler, A., Sandberg, R.D., Sandham, N.D., Pichler, R., Michelassi, V., Laskowski, G.: Direct numerical simulations of a high-pressure turbine vane. J. Turbomach. **138**, 7 (2016). https://doi.org/10.1115/1.4032435
49. Zhang, L., Kritioti, L., Wang, P., Zhang, J., Zangeneh, M.: A detailed loss analysis methodology for centrifugal compressors. J. Turbomach. **144**, 5 (2022). https://doi.org/10.1115/1.4054065
50. Aguirre, M.A., Duplaa, S., Carbonneau, X., Turnbull, A.: Velocity decomposition method for exergy-based drag prediction. AIAA J. **58**(11), 4686–4701 (2020). https://doi.org/10.2514/1.J059414
51. Schmitz, S.: Drag decomposition using partial-pressure fields in the compressible Navier–Stokes equations. AIAA J. **57**(5), 2030–2038 (2019). https://doi.org/10.2514/1.J057701
52. Mutangara, N.E., Sanders, D.S., Laskaridis, P., Hart, P.L., Schmitz, S.: A unified partial pressure field and velocity decomposition approach toward improved energetic aerodynamic force decompositions. In: 57th 3AF International Conference on Applied Aerodynamics, Bordeaux, France (2023)
53. Liou, M.-S., Kim, H., Liou, M.-F.: Challenges and progress in aerodynamic design of hybrid wingbody aircraft with embedded engines. Tech. Rep. TM-2016-218309, NASA (2016)

Publisher's Note Springer Nature remains neutral with regard to jurisdictional claims in published maps and institutional affiliations.



https://dspace.org/

Performance evaluation approach for design space explorations of propulsive fuselage aircraft concepts

Moirou, Nicolas G. M.; Sanders, Drewan S.

2025-04-01
Springer
https://doi.org/10.1007/s13272-025-00830-5
Moirou NGM, Sanders DS. (2025) Performance evaluation approach for design space explorations of propulsive fuselage aircraft concepts. CEAS Aeronautical Journal, Volume 16, April 2025, pp. 641-660

Downloaded from a DSpace repository. https://dspace.org/